

This is an Open Access document downloaded from ORCA, Cardiff University's institutional repository:<https://orca.cardiff.ac.uk/id/eprint/142908/>

This is the author's version of a work that was submitted to / accepted for publication.

Citation for final published version:

Cannizzaro, G., Wevers, T., Jonker, P.G., Pérez-Torres, M.A., Moldon, J., Mata-Sánchez, D., Leloudas, G., Pasham, D.R., Mattila, S., Arcavi, I., Decker French, K., Onori, F., Inserra, C., Nicholl, M., Gromadzki, M., Chen, T-W., Müller-Bravo, T.E., Short, P., Anderson, J.P., Young, D.R., Gendreau, K.C., Arzoumanian, Z., Löwenstein, M., Remillard, R., Roy, R. and Hiramatsu, D. 2021. Accretion disc cooling and narrow absorption lines in the tidal disruption event AT2019dsg. *Monthly Notices of the Royal Astronomical Society* 504 (1), pp. 792-815. 10.1093/mnras/stab851

Publishers page: <http://dx.doi.org/10.1093/mnras/stab851>


Please note:

Changes made as a result of publishing processes such as copy-editing, formatting and page numbers may not be reflected in this version. For the definitive version of this publication, please refer to the published source. You are advised to consult the publisher's version if you wish to cite this paper.

This version is being made available in accordance with publisher policies. See <http://orca.cf.ac.uk/policies.html> for usage policies. Copyright and moral rights for publications made available in ORCA are retained by the copyright holders.



# Accretion disc cooling and narrow absorption lines in the tidal disruption event AT 2019dsg

G. Cannizzaro<sup>1,2</sup> \*, T. Wevers<sup>3,4</sup>, P. G. Jonker<sup>2,1</sup>, M. A. Pérez-Torres<sup>5</sup>, J. Moldon<sup>5,6</sup>, D. Mata-Sánchez<sup>6</sup>, G. Leloudas<sup>7</sup>, D. R. Pasham<sup>8</sup>, S. Mattila<sup>9</sup>, I. Arcavi<sup>10,11</sup>, K. Decker French<sup>12</sup>, F. Onori<sup>13</sup>, C. Inserra<sup>14</sup>, M. Nicholl<sup>15,16</sup>, M. Gromadzki<sup>17</sup>, T.-W. Chen<sup>18</sup>, T. E. Müller-Bravo<sup>19</sup>, P. Short<sup>16</sup>, J. P. Anderson<sup>4</sup>, D. R. Young<sup>20</sup>, K. C. Gendreau<sup>21</sup>, Z. Arzoumanian<sup>21</sup>, M. Löwenstein<sup>21,22</sup>, R. Remillard<sup>8</sup>, R. Roy<sup>23</sup>, D. Hiramatsu<sup>24,25</sup>

<sup>1</sup>*SRON, Netherlands Institute for Space Research, Sorbonnelaan, 2, NL-3584CA Utrecht, the Netherlands*

<sup>2</sup>*Department of Astrophysics/IMAPP, Radboud University, P.O. Box 9010, 6500 GL Nijmegen, the Netherlands*

<sup>3</sup>*Institute of Astronomy, University of Cambridge, Madingley Road, Cambridge CB3 0HA, UK*

<sup>4</sup>*European Southern Observatory, Alonso de Córdova 3107, Casilla 19, Santiago, Chile*

<sup>5</sup>*Instituto de Astrofísica de Andalucía (CSIC), Glorieta de la Astronomía s/n, E-18080 Granada, Spain*

<sup>6</sup>*Jodrell Bank Centre for Astrophysics, School of Physics and Astronomy, The University of Manchester, Manchester, M13 9PL, UK*

<sup>7</sup>*DTU Space, National Space Institute, Technical University of Denmark, Elektrovej 327, 2800 Kgs. Lyngby, Denmark*

<sup>8</sup>*MIT Kavli Institute for Astrophysics and Space Research, Cambridge, MA 02139, USA*

<sup>9</sup>*Tuorla Observatory, Department of Physics and Astronomy, FI-20014 University of Turku, Finland*

<sup>10</sup>*The School of Physics and Astronomy, Tel Aviv University, Tel Aviv 69978, Israel*

<sup>11</sup>*CIFAR Azrieli Global Scholars program, CIFAR, Toronto, Canada*

<sup>12</sup>*Department of Astronomy, University of Illinois, Urbana IL, 61801, USA*

<sup>13</sup>*INAF - Osservatorio Astronomico d'Abruzzo via M. Maggini snc, I-64100 Teramo, Italy*

<sup>14</sup>*School of Physics & Astronomy, Cardiff University, Queens Buildings, The Parade, Cardiff, CF24 3AA, UK*

<sup>15</sup>*Birmingham Institute for Gravitational Wave Astronomy and School of Physics and Astronomy, University of Birmingham, Birmingham B15 2TT, UK*

<sup>16</sup>*Institute for Astronomy, University of Edinburgh, Royal Observatory, Blackford Hill, EH9 3HJ, UK*

<sup>17</sup>*Astronomical Observatory, University of Warsaw, Al. Ujazdowskie 4, 00-478 Warszawa, Poland*

<sup>18</sup>*The Oskar Klein Centre, Department of Astronomy, Stockholm University, AlbaNova, SE-10691 Stockholm, Sweden*

<sup>19</sup>*School of Physics and Astronomy, University of Southampton, Southampton, Hampshire, SO17 1BJ, UK*

<sup>20</sup>*Astrophysics Research Centre, School of Mathematics and Physics, Queens University Belfast, Belfast BT7 1NN, UK*

<sup>21</sup>*Astrophysics Science Division, NASA Goddard Space Flight Center, Greenbelt, MD 20771, USA*

<sup>22</sup>*Department of Astronomy, University of Maryland, College Park, MD 20742, USA*

<sup>23</sup>*The Inter-University Centre for Astronomy and Astrophysics, Ganeshkhind, Pune - 411007, India*

<sup>24</sup>*Las Cumbres Observatory, 6740 Cortona Drive, Suite 102, Goleta, CA 93117-5575, USA*

<sup>25</sup>*Department of Physics, University of California, Santa Barbara, CA 93106-9530, USA*

Accepted 2021 March 16. Received 2021 March 9; in original form 2020 October 22

## ABSTRACT

We present the results of a large multi-wavelength follow-up campaign of the Tidal Disruption Event (TDE) AT 2019dsg, focusing on low to high resolution optical spectroscopy, X-ray, and radio observations. The galaxy hosts a super massive black hole of mass  $(5.4 \pm 3.2) \times 10^6 M_{\odot}$  and careful analysis finds no evidence for the presence of an Active Galactic Nucleus, instead the TDE host galaxy shows narrow optical emission lines that likely arise from star formation activity. The transient is luminous in the X-rays, radio, UV and optical. The X-ray emission becomes undetected after  $\sim 125$  days, and the radio luminosity density starts to decay at frequencies above 5.4 GHz by  $\sim 180$  days. Optical emission line signatures of the TDE are present up to  $\sim 250$  days after the discovery of the transient. The medium to high resolution spectra show traces of absorption lines that we propose originate in the self-gravitating debris streams. At late times, after  $\sim 200$  days, narrow Fe lines appear in the spectra. The TDE was previously classified as N-strong, but after careful subtraction of the host galaxy's stellar contribution, we find no evidence for these N lines in the TDE spectrum, even though O Bowen lines are detected. The observed properties of the X-ray emission are fully consistent with the detection of the inner regions of a cooling accretion disc. The optical and radio properties are consistent with this central engine seen at a low inclination (i.e., seen from the poles).

**Key words:** Accretion:accretion discs – transients:tidal disruption events – galaxies:nuclei

## 1 INTRODUCTION

In the nuclear regions of a galaxy, a star whose orbital pericenter passes too close to the central supermassive black hole (SMBH) will be torn apart by the tidal forces (Hills 1975; Rees 1988; Evans & Kochanek 1989). During this so-called Tidal Disruption Event (TDE), roughly half of the stellar matter will spiral towards the SMBH, confined into self-gravitating streams (Guillochon et al. 2014) that can self-intersect and dissipate energy. This phenomenon gives rise to a luminous flare, typically peaking in the UV or soft X-rays, that can exceed the Eddington luminosity of the SMBH, over timescales of months to a year. While TDEs were originally discovered in the X-ray band (see Komossa 2002, for a review), recently significant numbers of TDE candidates are being discovered through wide field time domain optical surveys (e.g. Holoien et al. 2018; Leloudas et al. 2016; Blagorodnova et al. 2017; Wyrzykowski et al. 2017; Onori et al. 2019; Blagorodnova et al. 2019; van Velzen et al. 2020). The optical emission of TDEs has shown a wide variety of properties, but they are usually characterised by broad H and He emission lines (Arcavi et al. 2014), a strong blue continuum, black body (BB) temperatures of order  $10^4$  K and luminosities of order  $10^{44}$  erg s $^{-1}$ . A subset of TDEs have shown metal lines: either N and O lines (Blagorodnova et al. 2019; Leloudas et al. 2019; Onori et al. 2019) excited through the Bowen fluorescence mechanism (Bowen 1934, 1935) and/or low ionisation Fe lines (Wevers et al. 2019b). The presence/absence of H, He and N lines led to the phenomenological classification of van Velzen et al. (2020) into three classes: TDE-H, TDE-He and TDE-Bowen. There is no consensus on the origin of the optical emission of TDEs, be it either reprocessing of X-ray light through an atmosphere (Guillochon et al. 2014; Stone & Metzger 2016; Dai et al. 2018) or originating from shocks due to the self-intersections of the debris stream (Piran et al. 2015; Shiokawa et al. 2015; Bonnerot & Lu 2019).

While the presence of an accretion disc has been inferred also in optically selected TDEs, through the emergence of metal lines, double-peaked line profiles (Short et al. 2020; Hung et al. 2020) and their X-ray properties (Jonker et al. 2020; Wevers 2020), the TDE system has yet to be fully understood. This is hindered by the low numbers of TDE candidates (a few dozens), lack of high cadence, detailed spectroscopic monitoring, possible presence of reprocessing dust (Mattila et al. 2018), the presence of (non)relativistic radio outflows (see Alexander et al. 2020, for a review) and/or the dependency on the viewing angle of the observed properties (Dai et al. 2018; Nicholl et al. 2019a).

We present the analysis of an intensive follow-up campaign of AT 2019dsg, a nuclear transient discovered on 2019 April 09 by the Zwicky Transient Facility (ZTF)<sup>1</sup>, with the name ZTF19aapreis and subsequently classified as a TDE, at a magnitude  $r=18.9$ . The transient was discovered within a galaxy at a redshift  $z=0.0512$  (Nicholl et al. 2019b), which translates into a distance of  $D = 224$  Mpc (we do not consider uncertainties in the luminosity distance), assuming a cosmology with  $H_0=67.7$  km s $^{-1}$  Mpc $^{-1}$ ,  $\Omega_M=0.309$ ,  $\Omega_\Lambda=0.691$  (Planck Collaboration et al. 2014). In van Velzen et al. (2020) AT 2019dsg was studied as part of a larger sample of TDEs discovered by the ZTF. AT 2019dsg is categorised as a "TDE-Bowen" due to the perceived presence of H Balmer, He II as well as Bowen (N/O) fluorescence lines (Bowen 1934, 1935). The host galaxy of AT 2019dsg is in the "Green Valley" (Schawinski et al. 2014), a transition area of the colour-mass diagram between star-forming and quiescent galaxies. Galaxies in this region can show strong Balmer

lines and the post-starburst, E+A galaxies, which are known to be preferential hosts for TDEs (Arcavi et al. 2014; French et al. 2016), are also in this region. AT 2019dsg was also listed as a candidate counterpart for a neutrino event (Stein et al. 2019a). A study of the possible neutrino emission from AT 2019dsg and a more detailed analysis of the Spectral Energy Distribution (SED) is presented in Stein et al. (2020), where they propose a "multi-zone" model to explain the various emission components of the transient: a central engine for the X-ray emission, an UV/Optical photosphere and an outflow that powers the radio and neutrino emission. In this work, we focus on the X-ray emission and the optical spectra, on which we perform subtraction of the stellar component of the galaxy. Through this, we find that the N emission lines previously identified with the TDE are instead due to the host galaxy. Finally, in our medium and high resolution spectra, we find evidence for absorption lines, potentially due to the streams of disrupted stellar material. Throughout the paper, we use as a reference the discovery date of the transient: 2019 Apr 09 (MJD 58 582.46). All uncertainties are reported as  $1\sigma$ , unless stated otherwise.

## 2 OBSERVATIONS

### 2.1 Swift UVOT/XRT

AT 2019dsg was observed with the UVOT and XRT instruments on board the Neil Gehrels *Swift* satellite (Gehrels et al. 2004) with a cadence of around 3 days starting on 2019 May 21 (42 days after discovery) until 2019 Oct 15. We reduce and extract Swift/UVOT measurements using the UVOTSOURCE task in HEASOFT version 6.24. We use a standard 5 arcsec aperture to extract flux measurements, and a 50 arcsec aperture centred on an empty nearby region to estimate sky background levels. We correct for Galactic extinction assuming  $E(B-V) = 0.087$  (Schlafly & Finkbeiner 2011).

We use the online Swift/XRT pipeline tool<sup>2</sup> to reduce the X-ray data and determine source count rates in the 0.3–10 keV band, using the source optical coordinates. Due to the low number of counts, we create a single stacked spectrum with a total exposure time of 20 ks for spectral analysis.

### 2.2 NICER

Following the *Swift* detection of X-rays from AT 2019dsg, the Neutron star Interior Composition Explorer (*NICER*) (Gendreau et al. 2016) made several observations between 21 May 2019 and 6 June 2019. A second set of observations were obtained several months later (3-5 October 2019) in response to the IceCube alert of a neutrino detection from a sky region containing AT 2019dsg (Stein et al. 2019b). All observations of AT 2019dsg (OBSIDs: 200680101-2200680112) are reprocessed using the gain file *nxti-flightpi20170601v005.fits* by applying the *NICERL2 FT00L* with the default filtering criteria.

To build up statistics, data from observation IDs 2200680103-2200680104 and 2200680107-2200680108 are combined due to observational proximity in time and/or short exposure times. Observation IDs 2200680110-2200680112 are also combined. The total spectra for these seven groups are extracted and the background spectra are estimated using empirical background spectral libraries, constructed from observations of source-free areas of sky.

<sup>1</sup> <https://wis-tns.weizmann.ac.il/object/2019dsg/discovery-cert>

<sup>2</sup> [https://www.swift.ac.uk/user\\_objects/](https://www.swift.ac.uk/user_objects/)



## 2.3 Optical spectroscopic observations

### 2.3.1 WHT/ISIS

Observations of AT2019dsg were obtained with the Intermediate dispersion Spectrograph and Imaging System (ISIS) mounted at the Cassegrain focus of the William Herschel Telescope (WHT) in Roque de los Muchachos observatory (La Palma, Spain), Spain on 2019 August 22 under program SW19b01. Using a 1 arcsec slit in combination with the R600B grating provides wavelength coverage between 3600 and 5100 Å in the host rest frame, while the R600R grating covers the 6300 - 7800 Å range. The seeing was variable between 0.5 and 0.9 arcsec during the 2×2700s observations, leading to a seeing limited full width half maximum (FWHM) spectral resolution of  $\sim 94 \text{ km s}^{-1}$  (i.e.,  $\sigma_{instr} = 40 \text{ km s}^{-1}$ ), measured at  $\sim 4000 \text{ Å}$  from the arc frame. The observations were carried out with the slit at parallactic angle (Filippenko 1982) and with binning 1x1.

After performing the standard reduction tasks, such as a bias level subtraction and flat field correction, in IRAF (Tody 1986), we extract spectra using an extraction box with width of 1 arcsec in the spatial dimension. Wavelength solutions are applied using CuAr+CuNe arc frames obtained prior and after the science exposures. We combined the two exposures into a single, averaged spectrum using weights set to the average signal to noise ratio (SNR) of the individual spectra, and subsequently we fit cubic splines to normalise the averaged spectrum to the continuum (the spectra were not flux calibrated due to the absence of a standard star observation). A journal of the spectroscopic observations is presented in Table 1.

### 2.3.2 WHT/ACAM

AT2019dsg was observed several times with the Auxiliary-port CAMera (ACAM) low-resolution spectrograph mounted at the Cassegrain focus of the WHT under program W19AN003. The V400 grating in combination with the GG395A order-sorting filter provides a wavelength coverage of 3950–9400 Å and the resolution is  $R \sim 430$  and  $\sim 580$  for a 1.0 and 0.75 arcsec slit, respectively (from the technical manual of the instrument, measured at 5650 Å). The data were reduced using a pipeline based on standard IRAF data reductions procedures: flat field and bias correction, cosmic-ray cleaning, wavelength and flux calibration with arc lamps and standard stars. All observations were carried out with the slit at parallactic angle and with 1x1 binning.

### 2.3.3 TNG/DOLORES

We observed AT2019dsg twice with the Device Optimized for the LOw REsolution (DOLORES), installed at the Nasmyth B focus of the Telescopio Nazionale Galileo (TNG) in Roque de los Muchachos observatory (La Palma, Spain). The wavelength coverage of the LR-B grating is  $\sim 3000\text{--}8430 \text{ Å}$ , with a resolution  $R \sim 580$  for a 1.0 arcsec slit (nominal value, measured at 5850 Å). The slit was oriented at parallactic angle for all observations and the binning was 1x1. The spectra were reduced using standard IRAF procedures (bias and flat-field correction, wavelength and flux calibration with arc lamps and standard stars).

### 2.3.4 NTT/EFOSC2

Observations of AT2019dsg were carried out in the framework of the advanced Public ESO Spectroscopic Survey for Transient

Objects (ePESSTO+; Smartt et al. 2015), starting with the classification spectrum taken on 2019 May 13 (Nicholl et al. 2019b), with the ESO Faint Object Spectrograph and Camera v.2 (EFOSC2), an instrument for low resolution spectroscopy mounted at the Nasmyth B focus of the New Technology Telescope (NTT) at the La Silla observatory, Chile. All observations were performed using grism Gr#13, that provides a nominal wavelength coverage of 3685–9315 Å and a resolution with  $R \sim 355$  for a 1 arcsec slit, measured at 5600 Å (nominal value), with the slit at parallactic angle and with 1x1 binning. Data were reduced using pipelines based on standard IRAF tasks, such as bias and flat-field correction and wavelength and flux calibration using arc lamps and standard stars. When necessary, multiple spectra taken on the same night have been averaged with weights set to the mean value of the SNR of the individual exposures.

### 2.3.5 VLT/X-SHOOTER

We obtained one spectrum with the medium resolution spectrograph X-Shooter (Vernet et al. 2011), mounted at the Cassegrain focus of the second Unit Telescope (UT2) at the Very Large Telescope (VLT). X-shooter covers the wavelength range from 3000 to 25000 Å. The observation was carried out on 2019 August 29 with slit widths of 1.0, 0.9 and 0.9 arcsec for the UVB, VIS and NIR arms, respectively, with the slit oriented at parallactic angle. The set up used yields resolution of  $R \approx 5400$  (UVB),  $R \approx 8900$  (VIS) and  $R \approx 5600$  (NIR).s The data were reduced using the REFLEX X-shooter pipeline version 2.9.3 (Freudling et al. 2013) and are not flux calibrated. The spectra were also corrected for atmospheric absorption features using synthetic transmission spectra with the MOLECFIT software (Smette et al. 2015; Kausch et al. 2015). The NIR part of the spectrum shows no significant spectroscopic TDE signatures and is therefore not considered in this paper.

### 2.3.6 VLT/UVES

We observed AT2019dsg with the Ultraviolet and Visual Echelle Spectrograph (UVES), mounted at the Nasmyth B focus of UT2 at the VLT. The observation was carried out on 2019 Jul 04 with the standard central wavelengths of 346+580 nm (dichroic 1) and 437+860 nm (dichroic 2) that provide an almost full coverage of the 300 – 1060 nm wavelength range. With a 1 arcsec slit, the resolving power is  $\sim 40000$ . The data were reduced using the UVES pipeline (Ballester et al. 2000), adjusting the pipeline parameters where necessary.

### 2.3.7 Las Cumbres/FLOYDS

Las Cumbres Observatory (LCO) optical spectra were taken with the Folded Low Order whYte-pupil Double-dispersed Spectrograph (FLOYDS) mounted on the 2m Faulkes Telescope North (FTN) and South (FTS) at Haleakala (USA) and Siding Spring (Australia), respectively. A 2" slit was placed on the target at the parallactic angle. One-dimensional spectra were extracted, reduced, and calibrated following standard procedures using the FLOYDS pipeline<sup>3</sup> (Valenti et al. 2014). The FLOYDS spectra are not used in the analysis, due to a combination of low SNR, wavelength range covered

<sup>3</sup> [https://github.com/svalenti/FLOYDS\\_pipeline](https://github.com/svalenti/FLOYDS_pipeline)



**Table 1.** Spectroscopic observations

MJD <sup>(1)</sup> [days]	phase <sup>(2)</sup> [days]	UTC Date	Instrument	exposure time [s]	slit [″]
58 616.36	+34	2019 May 13	EFOSC2	900	1.0
58 631.13	+49	2019 May 27	DOLORES	1800	1.5
58 638.28	+55	2019 Jun 03	WFCCD	4x900	1.0
58 642.35	+60	2019 Jun 08	EFOSC2	1800	1.0
58 644.32	+62	2019 Jun 10	EFOSC2	2700	1.0
58 655.19	+73	2019 Jun 20	ACAM	1800	0.75
58 656.12	+74	2019 Jun 21	ACAM	1800	0.75
58 657.09	+75	2019 Jun 22	ACAM	1800	0.75
58 658.14	+76	2019 Jun 23	ACAM	1800	0.75
58 668.22	+86	2019 Jul 04	UVES	1800	1.0
58 676.19	+94	2019 Jul 12	ACAM	1800	1.0
58 678.10	+96	2019 Jul 13	ACAM	2x1800	1.0
58 689.25	+107	2019 Jul 25	EFOSC2	2700	1.0
58 690.11	+108	2019 Jul 25	ACAM	1800	0.75
58 692.12	+110	2019 Jul 27	ACAM	1800	1.0
58 710.94	+128	2019 Aug 15	ACAM	1800	1.0
58 715.88	+134	2019 Aug 20	ACAM	2x1800	1.0
58 717.00	+135	2019 Aug 21	ACAM	5x1800	1.0
58 717.89	+135	2019 Aug 22	ISIS	2x2700	1.0
58 724.14	+142	2019 Aug 29	XSH/UVB	4x920	1.0
58 724.14	+142	2019 Aug 29	XSH/VIS	4x920	0.9
58 724.14	+142	2019 Aug 29	XSH/NIR	8x480	0.9
58 733.93	+151	2019 Sep 07	ACAM	2x1800	1.0
58 735.96	+153	2019 Sep 09	ACAM	2x1800	0.75
58 777.02	+195	2019 Oct 10	EFOSC2	2x1800	1.5
58 808.04	+226	2019 Nov 21	EFOSC2	2100	1.0
58 824.83	+242	2019 Dec 07	ACAM	2200	1.5
58 827.82	+245	2019 Dec 10	ACAM	2700	1.5
58 994.12	+411	2020 May 24	DOLORES	2x2200	1.0

*Note.* (1) Modified Julian Day of observations; (2) calculated with respect to the discovery date MJD 58 582.

and proximity in time with higher quality spectra. Nonetheless, the spectra are reported in appendix (A).

### 2.3.8 *du Pont/WFCCD*

Observations were taken using the Wide Field reimaging CCD Camera (WFCCD) on the *du Pont* 100-inch telescope at Las Campanas Observatory using a 1 arcsec slit. The data were calibrated using HeNeAr arcs and bias subtraction, flat fielding and standard star observations for flux calibration. Reduction was performed with a modified version of `pyDIS` (Davenport et al. 2016) to extract and sky-subtract the spectrum.

For a journal of all the spectroscopic observations, see Table 1 and the complete sequence of spectra is shown in Fig. 1.

## 2.4 Optical photometric observations

### 2.4.1 *Las Cumbres Sinistro*

We observed AT2019dsg with the Las Cumbres Observatory Global Telescope Network (Brown et al. 2013). Observations were performed with the Sinistro cameras, mounted at the focus of 1-meter telescopes, at the following sites: South African Astronomical Observatory (CPT), Siding Spring Observatory (COJ), Cerro Tololo Interamerican Observatory (LSC) and McDonald Observatory (ELP). The target was observed with the Johnson B and V

filters and the Sloan filters *g*, *r*, *i*. Data was reduced with the `BANZAI` pipeline (McCully et al. 2018) which performs standard data reduction routines such as bad-pixel masking, bias frames subtraction, dark subtraction, flat field correction and cosmic rays correction. The zero points of the images were calibrated using the American Association of Variable Star Observers (AAVSO) Photometric All-Sky Survey (APASS) DR10 (Henden 2019). The magnitudes were estimated with aperture photometry, using the `IRAF` task `APPHOT`, with aperture sizes depending on the seeing conditions.

### 2.4.2 *LT IO:O*

We observed AT2019dsg using the Optical Wide Field camera (IO:O) at the Liverpool Telescope (LT) using the Sloan *g*, *r*, *i*, *z* and Johnson B and V filters. The images were reduced with the LT pipeline and the zeropoints calculated using stars in the APASS catalogue. Magnitudes were estimated through aperture photometry (`IRAF` task `APPHOT`), using apertures of variable size, depending on the seeing.

## 2.5 Radio observations: e-MERLIN

We observed our target source, AT2019dsg, with the e-MERLIN<sup>4</sup> radio interferometer in the UK between 2019 June 3 and September 12 (project code DD8006; PI Pérez-Torres). We observed AT2019dsg a total of 13 times: 10 at C-band (4.82–5.33 GHz) and 3 at L-band (1.25–1.77 GHz). We summarize in Table 2 the start time of each observing run and its duration at each frequency band. All observations had a total bandwidth of 512 MHz divided in eight spectral windows of 64 MHz with 512 channels per spectral window, except runs 07 through 10, which had four spectral windows of 128 MHz each. We used 3C286 and OQ208 as amplitude and bandpass calibrators, respectively. We correlated the phase calibrator, J2052+1619, at position  $\alpha_{J2000.0} = 20^{\text{h}}52^{\text{m}}43^{\text{s}}.6199$  and  $\delta_{J2000.0} = 16^{\circ}19'48''.828$ , which is separated 2.37 deg from our target, and we detected it clearly in all runs with a flux density of 0.32 Jy and 0.42 Jy at C and L-band, respectively.

We carried out all reduction steps using the e-MERLIN `CASA` pipeline<sup>5</sup> version v1.1.16 running on `CASA` (McMullin et al. 2007) version 5.6.2. We followed the default procedures of the pipeline using the default parameters, but adding manual flag commands to remove bad data that the pipeline could not remove. We used a common model for the phase reference calibrator to calibrate and image each run. We then used the `CASA` task `TCLEAN` to image the target source, using the e-MERLIN `CASA` pipeline imaging procedure with Briggs weighting and a robust parameter of 0.5 for all runs except numbers 03 and 07, which required robust 0.0 and -1.0, respectively, due to the lack of the longest baselines. The cell size was 8 mas for the C-band data and 20 mas for the L-band data. We show in Table 2 the synthesized beam size, local rms of the residual image, flux density and luminosity of the target source measured as the peak of emission of a Gaussian fit to the deconvolved image.

<sup>4</sup> <http://www.e-merlin.ac.uk/>

<sup>5</sup> <https://github.com/e-merlin/eMERLINCASApipeline>

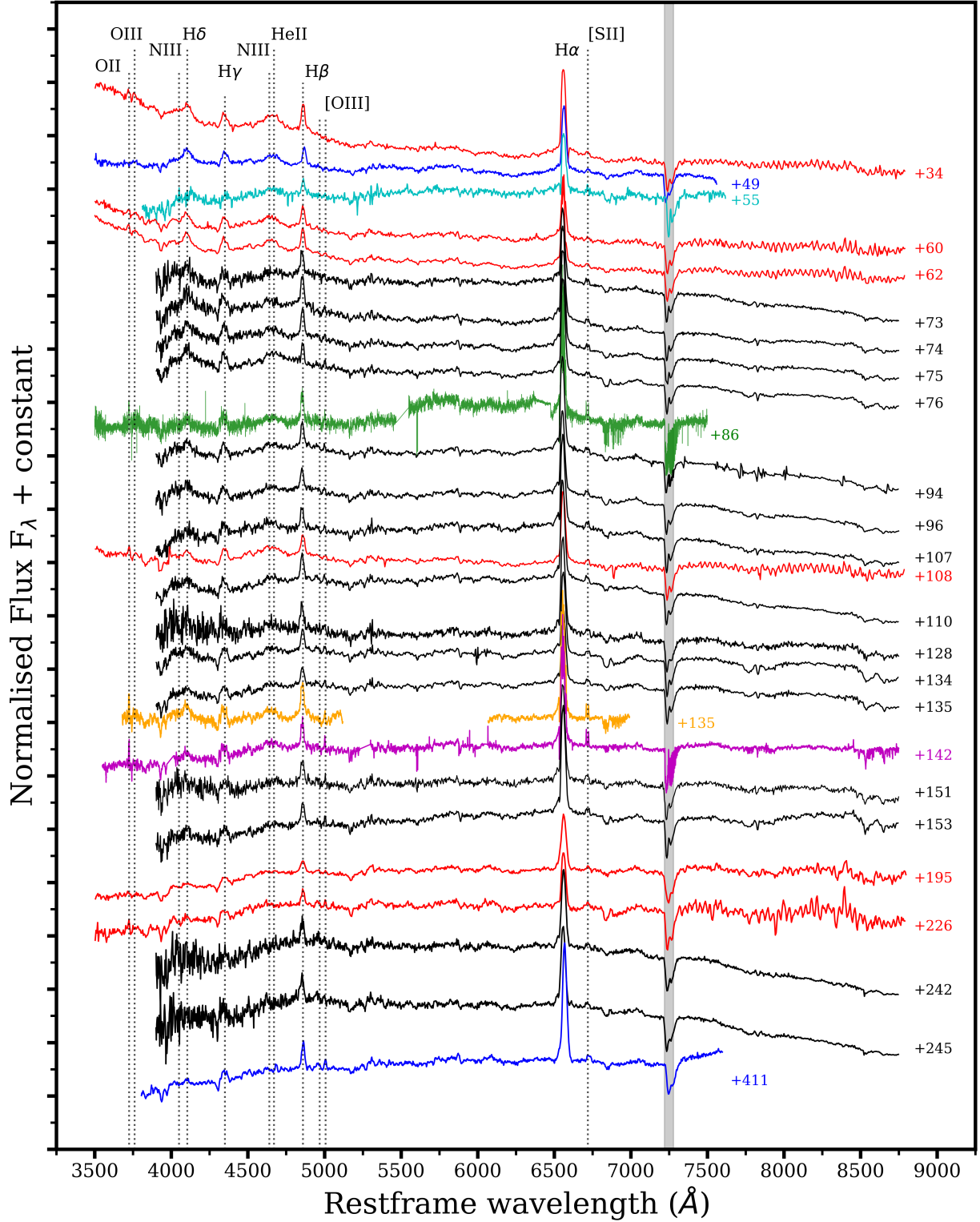


**Figure 1.** Sequence of spectra taken with EFOSC2 (red), DOLORES (blue), Du Pont (cyan), UVES (green), X-shooter (magenta), ISIS (orange) and ACAM (black). For each spectrum the phase with respect to the transient discovery date (2019 Apr 09, MJD 58582) is reported on the right. The dotted lines indicate the main emission lines and the grey band represents the area affected by telluric absorption. The H $\alpha$  line is affected by telluric absorption, but this is not shown in the plot for clarity. The UVES spectrum has been smoothed for clarity. All spectra have been corrected for foreground extinction. For plotting purposes, all spectra have been divided by their median value. The X-shooter, ISIS and UVES spectra are not flux calibrated.

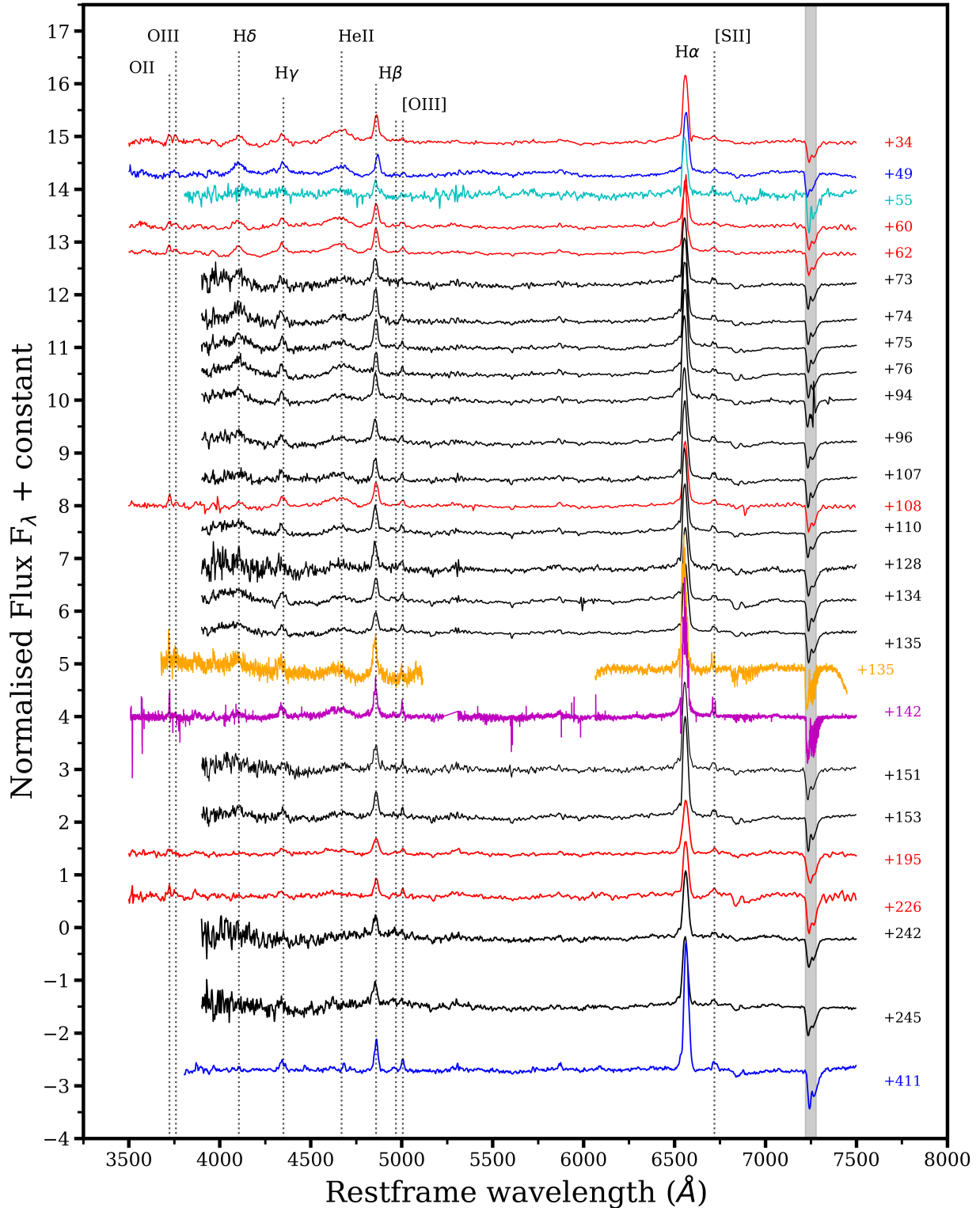


**Figure 2.** Sequence of host-subtracted spectra taken with EFOSC2 (red), DOLORES (blue), Du Pont (cyan), X-shooter (magenta), ISIS (orange) and ACAM (black). For each spectrum we annotate to the right the number of days passed since the transient discovery (2019 Apr 09, MJD 58 582). The dotted lines indicate the main emission lines and the grey band represents the area affected by telluric absorption, but this is not shown in the plot for clarity. All spectra have been corrected for foreground extinction. For plotting purposes, all spectra have been normalised. The X-shooter and ISIS spectra are not flux calibrated.



**Table 2.** Schedule of the e-MERLIN observations, with the run number, beam and total flux density at each frequency band. Values of the non-detections are  $3\text{-}\sigma$  level uncertainties with respect to the rms of the image. The last line is the  $4.1\sigma$  detection from the combined L-band data.

Run	MJD [days]	Start date	Duration [h]	Freq. [GHz]	Beam <sub>major</sub> [mas]	Beam <sub>minor</sub> [mas]	Beam <sub>pa</sub> [deg]	rms [ $\mu\text{Jy b}^{-1}$ ]	Flux density [ $\mu\text{Jy}$ ]	Luminosity [ $10^{37}\text{erg s}^{-1}$ ]
01	58 637.92	2019-06-03 22:00	12	5.1	67	32	28	32	$160 \pm 30$	$4.9 \pm 0.9$
02	58 654.88	2019-06-20 21:02	12	5.1	71	32	28	21	$340 \pm 20$	$10.4 \pm 0.6$
03	58 668.94	2019-07-04 22:32	10	5.1	764	580	76	86	$410 \pm 90$	$12.5 \pm 2.7$
04	58 669.94	2019-07-05 22:32	10	5.1	96	29	28	24	$460 \pm 20$	$14.1 \pm 0.6$
05	58 670.94	2019-07-06 22:32	10	5.1	98	30	27	23	$490 \pm 20$	$15.0 \pm 0.6$
06	58 671.94	2019-07-07 22:32	10	5.1	99	29	27	23	$480 \pm 20$	$14.7 \pm 0.6$
07	58 687.88	2019-07-23 21:17	10	5.1	177	54	14	128	$680 \pm 130$	$20.8 \pm 4.0$
08	58 691.89	2019-07-27 21:22	9	5.1	92	30	20	42	$650 \pm 40$	$19.9 \pm 1.2$
09	58 701.75	2019-08-06 18:00	11	5.1	69	33	25	27	$770 \pm 30$	$23.6 \pm 0.9$
10	58 738.68	2019-09-12 16:13	11	5.1	78	29	28	31	$1210 \pm 30$	$37.0 \pm 0.9$
11	58 688.88	2019-07-24 21:17	10	1.5	293	119	22	40	$< 120$	$< 1.1$
12	58 689.91	2019-07-25 21:50	9	1.5	322	115	21	44	$< 130$	$< 1.2$
13	58 690.89	2019-07-26 21:20	9	1.5	285	108	23	38	$< 115$	$< 1.0$
				1.5					$145 \pm 35$	$1.3 \pm 0.3$

### 3 ANALYSIS AND RESULTS

#### 3.1 e-MERLIN observations

The source is an unresolved point-like source in all detected epochs, with no significant hints of extended emission. We computed the statistical astrometric uncertainty as the standard deviation of the positions of the centroid fitted to the images, resulting in a relative astrometric accuracy of about 6 mas (6.5 pc). We measured no significant astrometric displacement from the C-band detections. The average position of AT2019dsg is  $\alpha_{J2000.0} = 20^{\text{h}}57^{\text{m}}02^{\text{s}}.9647$  and  $\delta_{J2000.0} = 14^{\circ}12'16''.305$ , as measured with respect to the phase reference correlation position quoted above. In L-band, we obtained  $3\sigma$  upper limits on the flux density. We therefore combined the data from the three consecutive days of observations in the L-band and found a point-like source that is spatially coincident with the source in the C-band images. We obtain a  $4\sigma$  detection of the source in the L-band with a flux density of  $145 \pm 35 \mu\text{Jy}$ , corresponding to a luminosity of  $1.3 \pm 0.3 \times 10^{37} \text{erg s}^{-1}$ .

We show in Fig. 3 the radio lightcurve of AT2019dsg for the first  $\sim 240$  days at multiple frequencies, including our e-MERLIN data. The e-MERLIN interferometer provides a better angular resolution than any of the other instruments. Therefore, the observed flux is not contaminated by background emission, so our observations provide bona fide flux densities against which to test the baseline of radio emission assumed in Stein et al. (2020). Overall, it appears that the agreement is good.

#### 3.2 Host velocity dispersion measurement

We use the X-shooter spectrum to constrain the width of the host galaxy absorption lines. In particular, we use the penalized pixel fitting routine `ppxf` (Cappellari 2017) to perform full spectrum template fitting with the Elodie stellar template library (Prugniel & Soubiran 2001). We resample the X-shooter spectrum within the errors and measure velocity dispersions for 1000 realisations of the data (see Wevers et al. 2017 for a detailed explanation of the method). Fitting the resulting velocity dispersion distribution with a Gaussian model, we find a mean FWHM of  $94 \text{ km s}^{-1}$  with a standard deviation of  $1 \text{ km s}^{-1}$ , which we adopt as the velocity dispersion and its measurement uncertainty. Using the  $M\text{-}\sigma$  relation

of Gültekin et al. (2009) and adding the measurement errors linearly with the scatter in the relation, this corresponds to a black hole mass of  $\log(M_{\text{BH}}) = 6.73 \pm 0.40 M_{\odot}$ . We note that by using both the  $M$ -sigma relations of Ferrarese & Ford (2005) and of McConnell & Ma (2013), we obtain a value for the black hole mass which is compatible with the previous estimate within uncertainties. This corresponds to an Eddington luminosity  $L_{\text{Edd}} = (6.8 \pm 4.1) \times 10^{44} \text{erg s}^{-1}$  and a Schwarzschild radius of  $R_{\text{S}} = (1.6 \pm 0.9) \times 10^{13} \text{cm}$ , for a non-rotating BH.

#### 3.3 UV/optical lightcurve

The host galaxy is marginally detected in the GALEX NUV band ( $\lambda_{\text{cen}} = 2328 \text{ \AA}$ ;  $\text{NUV} = 21.1 \pm 0.4$ ), indicating that even in the latest epochs (190 days after discovery) when the source was detected at a magnitude of UVM2 ( $\lambda_{\text{cen}} = 2260 \text{ \AA}$ ) = 18.95, host contamination is not an issue in the UV bands. To check the host galaxy contamination in the optical, we use the Kron magnitudes from Pan-STARRS (PS) Data Release 2, using the filter transformations from Jordi et al. (2006), when necessary.

In the optical, the transient is detected above the host galaxy light in the U band, and in B and g only for the first  $\sim 80$  days of observation. We then remove the host galaxy contribution by subtracting the flux derived from the Kron magnitudes from PS. We plot the host-subtracted UV/optical light curve in Fig. 4 (only magnitudes above the galaxy light are plotted) and the observed magnitudes are reported in Table C1.

##### 3.3.1 UV/optical blackbody fitting

Since in most of our additional photometric observations the transient light is not detected above the host galaxy level, we do not create an SED for the source, but we use the results from van Velzen et al. (2020) and Stein et al. (2020). They find that the UV/optical lightcurve is well fit by a blackbody with roughly constant temperature  $T = (3.9 \pm 0.2) \times 10^4 \text{ K}$  and radius  $R = (3.9 \pm 0.3) \times 10^{14} \text{ cm}$ . The maximum bolometric luminosity is  $L_{\text{bb}} = (2.9 \pm 0.3) \times 10^{44} \text{erg s}^{-1} \sim 0.4 L_{\text{Edd}}$ .

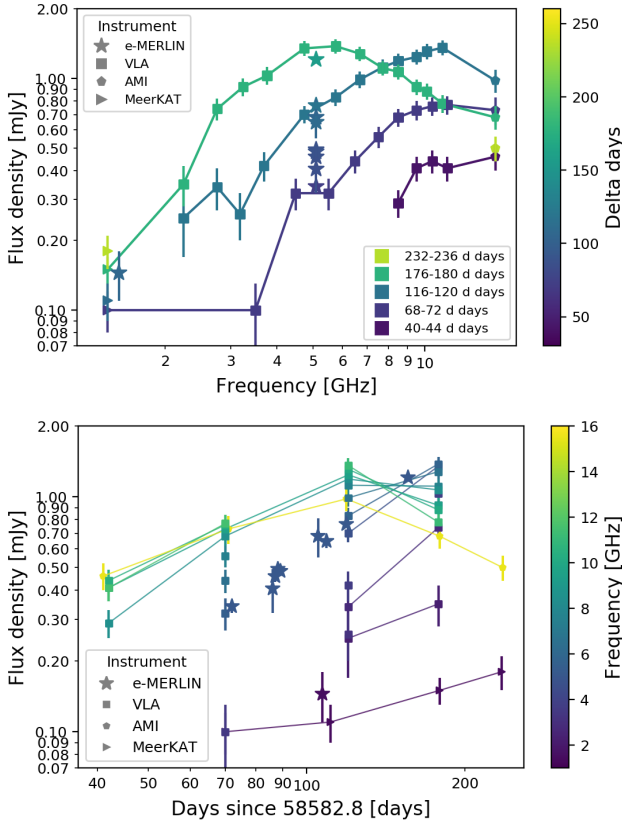


**Figure 3.** Radio evolution of AT2019dsg. VLA, AMI, and MeerKAT data are from Stein et al. (2020), while e-MERLIN data (stars) are our own data. The e-MERLIN data are not connected by solid lines for readability. Note the characteristic synchrotron shift of the peak frequency with time, so by day  $\sim 180$  the radio emission at frequencies above  $\sim 6.0$  GHz is already in its optically thin, decaying phase, while at smaller frequencies is still in its optically thick, increasing phase.

### 3.4 X-ray spectral analysis

#### 3.4.1 *Swift*/XRT

To fit the *Swift* X-ray spectrum we use XSPEC 12.10.0 (Arnaud 1996) in HEASOFT v6.24, and assume a Galactic column density of  $n_H = 6.45 \times 10^{20} \text{ cm}^{-2}$  (HI4PI Collaboration et al. 2016). Due to the low number of counts in each bin, we use Cash statistics (the results are identical when rebinning the spectrum to 20 counts/bin and using Gaussian statistics). Confidence intervals are quoted at the 90 per cent level ( $\Delta C\text{-stat}=2.71$ ). A  $65 \pm 6$  eV blackbody model (TBabs  $\times$  zashift  $\times$  bbbodyrad) provides a good fit to the data (cstat = 137 for 682 dof or  $\chi^2=0.81$  with 9 dof), with a radius  $R = 3.4^{+1.5}_{-0.9} \times 10^{11}$  cm. Using instead a multi-temperature blackbody model (diskbb) yields  $kT = 80 \pm 7$  eV (cstat = 135 for 682 dof). These results are in agreement with those presented in Stein et al. (2020). To convert the count rates to unabsorbed 0.3–10 keV fluxes, we assume the simple blackbody model with Galactic extinction, which gives a conversion factor of  $9.1 \times 10^{-11} \text{ cts/erg/cm}^2/\text{s}$ .

#### 3.4.2 *NICER*

Background-subtracted *NICER* spectra are fit to the same absorbed, redshifted blackbody model used for the *Swift*/XRT spectrum. The source is not detected over the *NICER* background above 1 keV,

and fits are conducted in the 0.3–1 keV bandpass, with luminosities and count rates referring to this energy range. The latest effective area (*nixtiaveonaxis20170601v004.arf*) and response matrix (*nixtiref20170601v002.rmf*) files are utilized. The blackbody temperature for the late-time spectrum is fixed at 30 eV. The results are shown in Table 3, and are consistent with the analysis of the *Swift*/XRT spectrum.

The 0.3–10 keV X-ray lightcurve is shown in Fig. 5, where we have used the webPIMMS<sup>6</sup> tool to convert the *NICER* 0.3–1 keV luminosities to the 0.3–10 keV energy range for consistency with the XRT data. The X-ray luminosity shows a rapid decay from  $3 \times 10^{43} \text{ erg s}^{-1}$  to  $10^{42} \text{ erg s}^{-1}$  over 25 days. Then, the decay becomes more shallow and the X-ray luminosity reaches  $3.6 \times 10^{41} \text{ erg s}^{-1}$  in the last epoch at which the source is detected (125 days after the discovery of the transient). The XRT light curve shows variability of factor 2–3 on a timescale of days during the initial rapid decrease, while this behaviour is not seen in the *NICER* data. In Fig. 6, we plot the evolution of the BB temperature with time. The temperature decreases from 70 eV to 40 eV over  $\sim 15$  days. In Fig. 7 we plot the 0.3–1 keV X-ray luminosity versus the BB temperature from the fit to the *NICER* data. We overplot the data with a  $L_X \propto T^4$  curve.

### 3.5 Optical spectroscopy

The sequence of spectra from EFOSC2, DOLORES, UVES, X-shooter, ISIS and ACAM is shown in Fig. 1. The first spectra show a blue continuum that decays over time. The decay of the blue part of the spectrum pivots around  $5000 \text{ \AA}$ . The continuum is dominated by the host galaxy redwards of this wavelength at all stages of the TDE outburst. After roughly 60 days, the blue continuum light has decayed. Coincidentally, this is similar to the timescale over which the X-ray flux becomes undetectable. The spectra show strong Balmer emission lines ( $H\alpha$  through  $H\delta$ ) and a broad He II emission line that becomes less visible with respect to the surrounding continuum over time. We also identify the O II doublet at  $3726$  and  $3729 \text{ \AA}$  and O III at  $3760 \text{ \AA}$  in emission.

#### 3.5.1 *Subtraction of the stellar component*

The spectra clearly show absorption features due to the host galaxy, more prominently in the medium-high resolution spectra. To remove the stellar contribution, we employ PPF: we build a synthetic host galaxy spectrum by fitting stellar spectra to our X-shooter spectrum. The method convolves a series of stellar template spectra to the observed spectrum (host galaxy+TDE), by combining the individual stellar templates with additive and/or multiplicative orthogonal polynomials and an initial guess of the line of sight velocity dispersion (LOSVD). The best fitting template (or combination of templates) is then found by  $\chi^2$  minimization. The emission features and areas affected by telluric absorption are masked during the template convolution procedure. This method therefore removes from the observed spectra the stellar component from the host galaxy. We employ the PHOENIX high-resolution synthetic spectral library<sup>7</sup> (Husser et al. 2013); this library covers the whole wavelength range of the UVB and VIS arms of X-shooter ( $3000 - 10000 \text{ \AA}$ ) with a resolution of  $R \sim 50000$ . Of the whole library, which contains  $\sim 30000$  synthetic spectra covering a broad range of stellar properties, we

<sup>6</sup> <https://heasarc.gsfc.nasa.gov/cgi-bin/Tools/w3pimms/w3pimms.pl>

<sup>7</sup> <http://phoenix.astro.physik.uni-goettingen.de/>

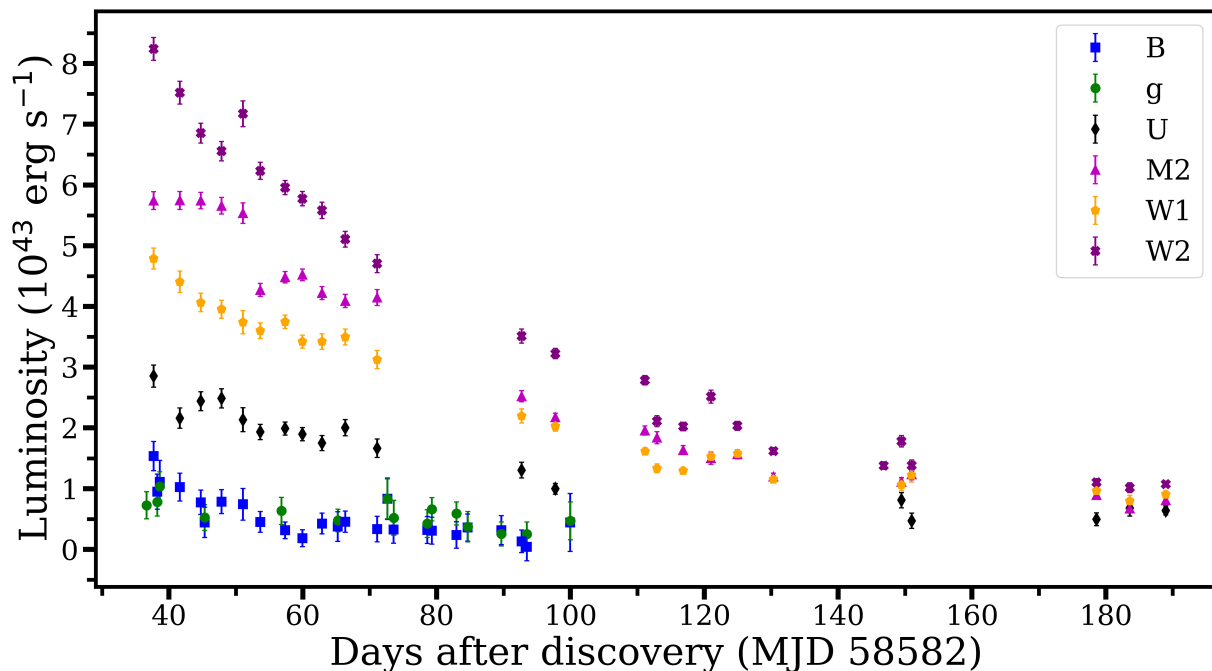


**Figure 4.** Host-subtracted light curve of AT2019dsg : B (blue squares), g (green circles), U (black diamonds), UVM2 (magenta triangles), UVW1 (orange pentagons) and UVW2 (purple crosses).

ObsIDs	0.3–1 keV count rate (cts s <sup>-1</sup> )	Average Time (MJD)	Exposure (seconds)	kT (eV)	c-statistic	Degrees of freedom	Luminosity (10 <sup>42</sup> erg s <sup>-1</sup> )
200680102	2.02	58 625.8	2159	68±1	82.19	67	32.5 <sup>+1.0</sup> <sub>-0.9</sub>
200680103-4	1.71	58 630.3	767	67±2	46.54	67	28.1 <sup>+1.6</sup> <sub>-1.5</sub>
200680105	1.48	58 633.16	593	65±3	75.54	67	25.0 <sup>+2.0</sup> <sub>-1.7</sub>
200680106	1.09	58 634.06	627	63±3	58.86	67	18.9 <sup>+1.5</sup> <sub>-1.4</sub>
200680107-8	0.4	58 639.21	239	43 <sup>+8</sup> <sub>-7</sub>	55.26	67	9.8 <sup>+2.5</sup> <sub>-2.11</sub>
200680110-12	0.02	58 759.99	15493	30	108.7	68	<0.63

**Table 3.** Best-fit model parameters derived from time-resolved *NICER* X-ray (0.3–1 keV) spectra. The temperature in the last epoch is kept fixed at 30 eV and the luminosity value is a  $3\sigma$  upper limit.

select a subsample with effective temperature  $2300 \text{ K} \leq T_{eff} \leq 12000 \text{ K}$ , metallicity in range  $-2.0 \leq [\text{Fe}/\text{H}] \leq 1.0$  and alpha elements abundance  $[\alpha/\text{Fe}] = 0$ . This library does not contain emission line templates. We use the X-shooter spectrum as a basis for building our synthetic host galaxy spectrum as it is the highest resolution spectrum on which we can apply the `PPXF` routine: the ISIS spectrum does not have enough continuum free from emission features and the continuum of the UVES spectrum has too low a SNR to make the routine converge. We then use again the `PPXF` code to scale the synthetic host spectrum to the other spectra of our follow-up. Since this is not possible for spectra with a higher resolution, we did not perform the subtraction on the UVES spectrum. After the subtraction, the continuum of the spectra is scaled to 1, using the median of the flux.

The host subtracted spectra (shown in Fig. 2) still show strong H $\alpha$  and H $\beta$  emission lines, both with a broad (FWHM  $\sim 5000$ – $10000 \text{ km s}^{-1}$ ) component at the base, and a narrower (FWHM  $\sim 1000 \text{ km s}^{-1}$ ) peak. Due to the redshift of the host galaxy, the H $\alpha$  line is contaminated by the telluric absorption band at  $\sim 6900 \text{ \AA}$ . This

is most clearly visible in the ISIS, UVES and X-shooter spectra, due to the higher resolution of these spectra. Redwards of H $\alpha$ , the two [S II] lines (6716 and 6731  $\text{\AA}$ ) are visible and resolved in some spectra. The H $\gamma$ , H $\delta$  and the broad He II lines are still detected and the [O III] doublet (4959, 5007  $\text{\AA}$ ) becomes clearly visible. Also the O II doublet (3726, 3729  $\text{\AA}$ ) and a weak O III at 3760  $\text{\AA}$  are still detected. We fit the emission lines of the host subtracted spectra with multiple Gaussian components, combined with a polynomial to fit the local continuum, using PYTHON code employing the `LMFIT`<sup>8</sup> package (Newville et al. 2014). During the fitting procedure, we tied the FWHM and the separation of the [S II] lines and of the [O III] lines, when the doublets were resolved. The central wavelengths of the broad base and the narrow peak of H $\beta$  are also tied together, to reduce the number of free parameters in this region. We were not able to fit the [N II] doublet at 6548 and 6583  $\text{\AA}$ , probably due to the presence of the telluric absorption. Example H $\alpha$  and H $\beta$  line fits are shown in Fig. 8 and 9, respectively.

<sup>8</sup> <https://lmfit.github.io/lmfit-py/>



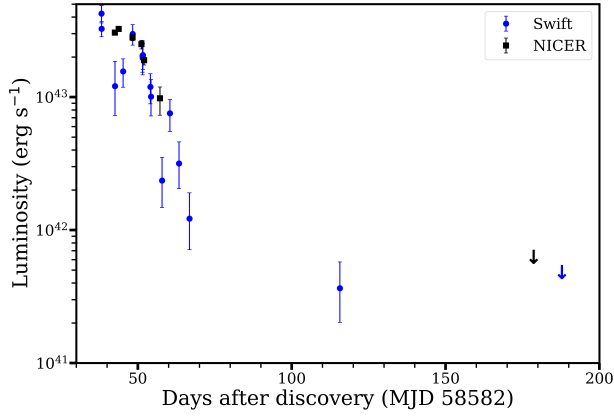


**Figure 5.** The 0.3–10 keV X-ray luminosity evolution with time of AT 2019dsg. In blue (circles for detections), the Swift data, in black (squares for detections), the NICER data. The downward arrows represent  $3\sigma$  upper limits.

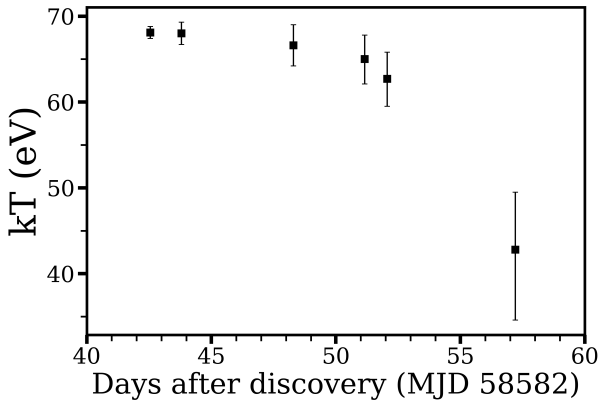


**Figure 6.** Evolution of the BB temperature from the fit to the NICER (0.3–1 keV) data with time.

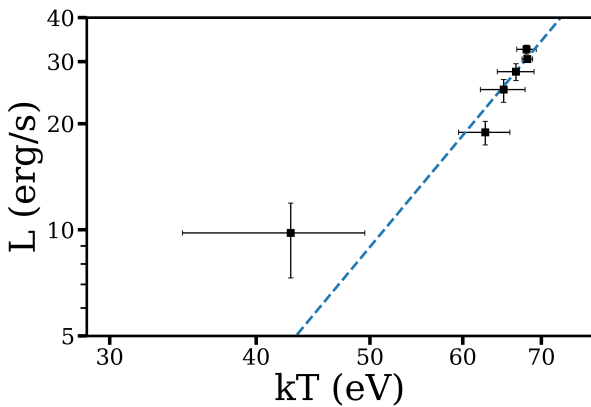


**Figure 7.** X-ray luminosity (0.3–1 keV) versus the BB temperature. The dashed line represents  $L \propto kT^4$  with arbitrary normalisation. The observed rate of cooling decreases over time.

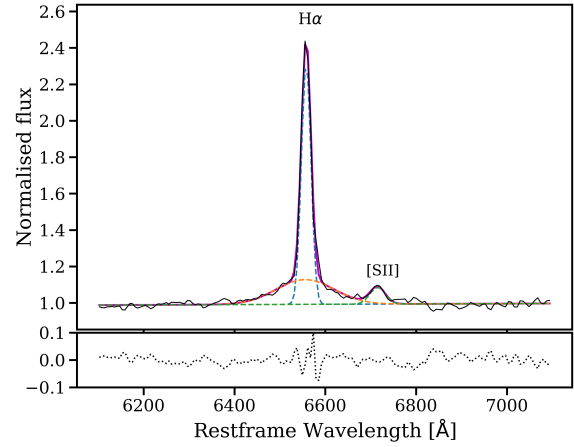


**Figure 8.** Example of the fit to the  $H\alpha$  and  $[S II]$  emission lines in the EFOSC2 spectrum taken on 2019 June 10 (62 days after discovery), after performing the host galaxy subtraction. The dashed lines represent different Gaussian components, while the solid line represents the total fitting function. In the bottom panel, the residuals of the fit.

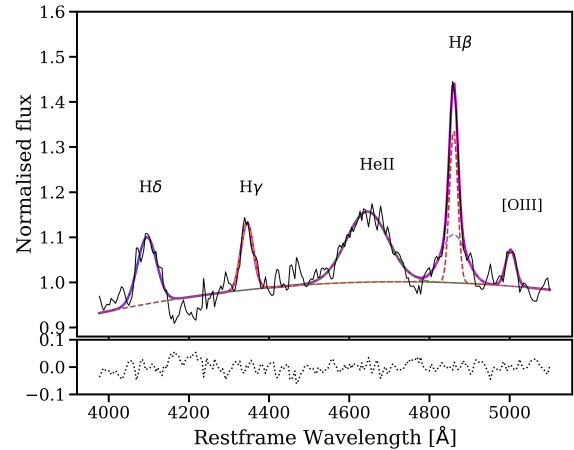


**Figure 9.** Example of the fit to the emission lines in the  $H\beta$  region of the EFOSC2 spectrum taken on 2019 June 08 (60 days after discovery), after the subtraction of the stellar component process. The dashed lines represent different Gaussian components, while the solid line represents the total fitting function. In the bottom panel, the residuals of the fit.

After the subtraction procedure, from the spectrum of 2019 September 09 (153 days after discovery) onward, the broad bases of  $H\alpha$  and  $H\beta$  are not detected anymore. The  $He II$  line is not detected after the spectrum of 2019 November 21 (226 days after discovery). We therefore associate these lines with the transient event, while we consider the remaining, more narrow, emission features as due to star formation in the host galaxy instead (see Sec. 4.1). At late times (more than 200 days after discovery), in the continuum between  $H\beta$  and  $H\alpha$ , metal lines appear. In Fig. 10, we show a comparison between AT 2019dsg and two other TDEs that have shown metal lines in the same wavelength range during their evolution: ASASSN-15oi and AT2018fyk (Wevers et al. 2019b). In the spectrum of AT 2019dsg we can clearly identify absorption lines

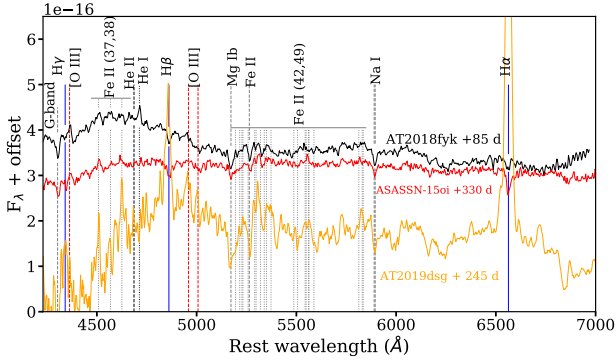


**Figure 10.** Comparison between the spectra of AT2019dsg (orange) at +245 days and AT2018fyk (black) at +85 days and ASASSN 15oi (red) at +330 days, the other two TDES that have shown Fe lines in their optical spectra.

from Na I and Mg Ib and many emission lines from Fe II, as well as the Fe II absorption feature at 5264 Å.

We took a late time spectrum with TNG on 2020 May 24 (411 days after discovery, last spectrum of Fig. 1 and 2), after the object came back from behind the Sun. In this spectrum we clearly see the narrow H $\alpha$  and H $\beta$ , [O III] and [S II] lines, a still strong H $\gamma$  and weak H $\delta$  emission lines. The aforementioned metal lines are not present in this spectrum.

### 3.5.2 X-shooter, ISIS and absorption lines

The H $\beta$  region of the X-shooter spectrum is plotted in Fig. 11. The spectrum shows the [O III] doublet (4959 and 5007 Å), the H $\beta$  line with the usual two components, the broad He II, and the H $\gamma$  line. The H $\gamma$  emission line shows an absorption line superimposed and the He II shows two absorption features.

The host subtracted ISIS spectrum shows a similar morphology, albeit the absorption features in the He II line are less pronounced. The fit to the H $\gamma$  and He II emission lines of the ISIS spectrum is shown in Fig. 12. The absorption lines on top of the H $\gamma$  and He II emission lines are present in both the original spectrum, before the subtraction of the host galaxy light, and in the host-subtracted one. The FWHM, equivalent width (EW) and central wavelength of these absorption lines are reported in Table 4. The absorption line parameters are within uncertainties between the two spectra.

The resolution in the spectra obtained during the remainder of our follow-up campaign is not high enough to investigate these absorption features in detail (we will discuss the UVES spectrum separately in Sec. 3.5.4). In both the ISIS and X-shooter spectra, the H $\alpha$  line is strongly affected by the atmospheric absorption that we were not able to correct completely with MOLECFIT (see Sec. 2.3.5), therefore a precise fit of the H $\alpha$  line was not possible. Nonetheless, in the host-subtracted spectra, the two [S II] lines (6716 and 6731 Å) are clearly detected and resolved. In the lower resolution spectra of our follow-up campaign, the two lines often blend together.

### 3.5.3 Line fitting results

We report the results of the line fitting in Tables B1, B2 and B3. We plot the evolution of the line parameters resulting from the fit: the FWHM, equivalent width (EW) and shift with respect to the rest frame wavelength are shown in Figures 13, 14 and 15, respectively.

**Table 4.** H $\gamma$  and He II absorption lines

	H $\gamma$	He II	He II
FWHM <sub>I</sub>	829 ± 128	656 ± 140	983 ± 317
FWHM <sub>X</sub>	649 ± 39	1065 ± 50	757 ± 42
EW <sub>I</sub>	-2.6 ± 0.6	-1.1 ± 0.3	-1.0 ± 0.4
EW <sub>X</sub>	-1.4 ± 0.1	-2.5 ± 0.2	-1.4 ± 0.1
WL <sub>I</sub>	4348.3 ± 0.6	4639.2 ± 0.8	4658.8 ± 1.6
WL <sub>X</sub>	4349.1 ± 0.2	4641.9 ± 0.3	4662.1 ± 0.3

*Note.* FWHM (in km s<sup>-1</sup>), EW (in Å) and central wavelength (WL, in Å) of the absorption lines superimposed the H $\gamma$  and He II emission lines in the X-shooter and ISIS spectra (Fig. 11 and 12, respectively). With I we indicate the results from the fit to the ISIS spectrum (135 days after discovery) and with X the ones from the X-shooter spectrum (142 days after discovery). The values have been corrected for the instrumental broadening.

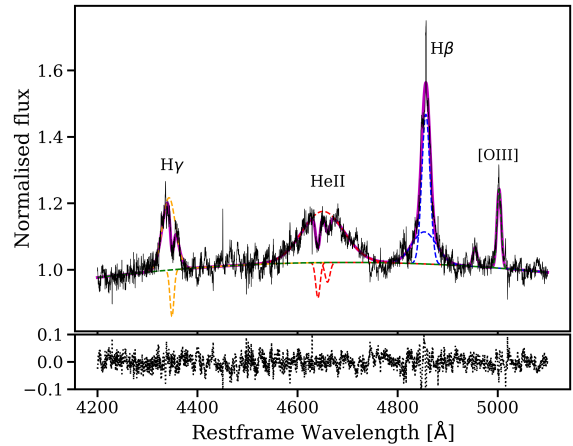


**Figure 11.** Fit to the emission lines in the H $\beta$  region of the host galaxy subtracted X-shooter spectrum obtained 142 days after discovery of AT2019dsg. The dashed lines represent different Gaussian components, while the solid line represents the total fitting function. In the bottom panel, the residuals of the fit.

The values of the FWHM have been corrected for the instrumental broadening, measured from the sky lines of the spectra. The FWHM (Fig. 13) of the broad components of H $\alpha$  and H $\beta$  have different values but a similar evolution. The FWHM of the broad H $\alpha$  starts at 12000 km s<sup>-1</sup>, decreases to almost 5000 km s<sup>-1</sup> over 30 days and then increases to the initial value of 12000 km s<sup>-1</sup> in ~20 days, to stay at this value until it is no longer detected, 150 days after the discovery of the transient. The FWHM of the broad H $\beta$  has an initial value around 5000 km s<sup>-1</sup>, and for the whole duration of the follow-up campaign fluctuates between 4000 and 8000 km s<sup>-1</sup>. There are some significant outliers that could be due to the corresponding spectra having a low signal to noise ratio (SNR), while others could be caused by variations due to uncertainties in the subtraction process. The initial evolution of the FWHM of H $\gamma$  is similar to the one observed for the broad H $\alpha$  (albeit with lower values): it starts at 3500 km s<sup>-1</sup>, to then decrease to 2000 km s<sup>-1</sup> over 30 days. It then remains around this value until the end of our follow-up campaign. The H $\delta$  line in all the ACAM spectra is not well constrained, because it falls at the edge of the wavelength range covered. There-

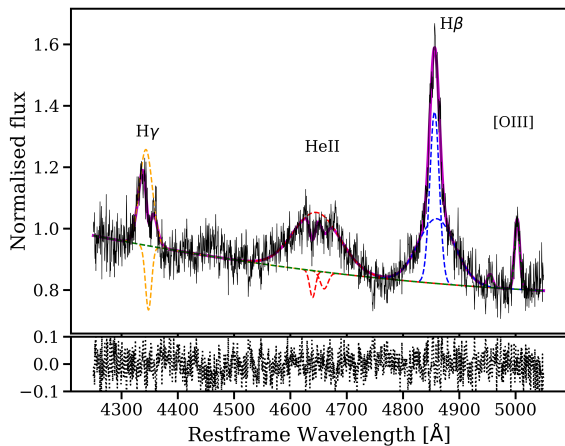


**Figure 12.** Fit to the emission lines in the H $\beta$  region of the host galaxy subtracted ISIS spectrum obtained 135 days after discovery of AT 2019dsg. The dashed lines represent different Gaussian components, while the solid line represents the total fitting function. In the bottom panel, the residuals of the fit.

fore we do not fit it at these epochs. Its FWHM has an initial value similar to the one of H $\gamma$  at  $4000 \text{ km s}^{-1}$ , it then increases to  $4500 \text{ km s}^{-1}$  at the next epoch (20 days later), to then gradually decrease to  $3000 \text{ km s}^{-1}$  between phase 60 and 110. The FWHM of He II goes from  $10000 \text{ km s}^{-1}$  to  $5500 \text{ km s}^{-1}$  in the first 30 days, then increases up to  $10000 \text{ km s}^{-1}$  in 30 days, to then decrease to  $7000 \text{ km s}^{-1}$  between 80 and 160 days. In the last two epochs, the FWHM of He II increases up to  $13000 \text{ km s}^{-1}$ . The timescale of the initial decay of the FWHM of the broad H $\alpha$ , H $\beta$ , and the He II is similar to the timescale of the decay of the X-ray light and of the blue continuum. Finally, the FWHMs of the narrow peaks of H $\alpha$  and H $\beta$  do not show evolution over the time of observation and vary around  $1000 \text{ km s}^{-1}$ , except for two outliers at 195 and 225 days after discovery, when the narrow H $\beta$  has a FWHM above  $1500 \text{ km s}^{-1}$ . These points are due to the low SNR of the corresponding spectra. The values of the FWHM of the narrow H $\alpha$  and H $\beta$  peaks obtained from the late time spectrum (411 days after discovery) are both around  $1200 \text{ km s}^{-1}$ .

In Fig. 14 we plot the evolution of the EW of the emission lines with time. The EW of the broad base of H $\alpha$  decreases from an initial value of  $35 \text{ \AA}$  to  $20 \text{ \AA}$  in 30 days, then increases to  $40 \text{ \AA}$  at phase +80, to then decrease again to  $25 \text{ \AA}$  over the rest of the follow-up campaign, except for the last epoch, when the EW is at  $35 \text{ \AA}$ . The EW of the broad base of H $\beta$  varies between  $5$  and  $20 \text{ \AA}$ , to then stabilise around  $10 \text{ \AA}$  in the last  $\sim 40$  days. The higher values are also in this case due to low SNR and uncertainties during the subtraction process, rather than being indicative of variability in the line. The EW of the H $\gamma$  line starts at  $10 \text{ \AA}$ , to then decrease to  $5 \text{ \AA}$  after 30 days. It subsequently remains constant until the last two epochs in which the EW is  $4 \text{ \AA}$ . The H $\delta$  line follows a very similar evolution, except for the value at 50 days after discovery. The EW of the He II has an initial value of  $40 \text{ \AA}$  and, already 20 days after this (50 days after discovery), it decreases to  $10 \text{ \AA}$ , where it remains almost constant for the next 100 days. The outliers at 80 and 110 days, with an EW above  $30 \text{ \AA}$ , are possibly due to uncertainties in the subtraction process. The initial evolution matches the time-scale of the decay of the blue continuum of the TDE. Finally, the EW of the narrow H $\beta$  remains constant around  $10 \text{ \AA}$ , while the EW of the

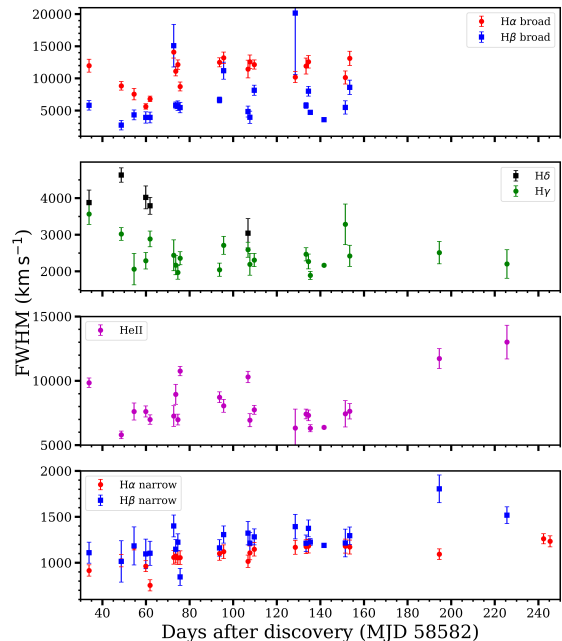


**Figure 13.** Evolution of the FWHM of the emission lines. In the first panel, the broad base of H $\alpha$  (red circles) and H $\beta$  (blue squares); in the second panel, H $\gamma$  (green circles) and H $\delta$  (black squares); third panel, He II (magenta circles). These three lines are due to the TDE. In the bottom panel, the narrow peaks of H $\alpha$  (red circles) and H $\beta$  (blue squares) are shown, these lines are due to host galaxy activity. On the x-axis, the number of days passed since the discovery of the transient.

narrow H $\alpha$  varies around  $40 \text{ \AA}$ . The small scale variations of the H $\alpha$  narrow peak are likely due to variations of the telluric absorption.

We plot the shift with respect to the restframe wavelength of the emission lines in Fig. 15 (we indicate blue shifts with negative values). To reduce the number of free parameters, during the fitting procedure, the central wavelength of the broad H $\beta$  was tied to the one of the narrow peak, which, due to the high SNR in that line, dominates the fit result of this parameter (we do not show the shift of the broad H $\beta$  in the plot). The broad H $\alpha$  shows a blue shift that fluctuates between  $0$  and  $-2000 \text{ km s}^{-1}$ , without a clear evolution with time. The He II line is blueshifted by  $-2000 \text{ km s}^{-1}$  at the first epoch of observation. The value of the shift fluctuates around this value for the first  $\sim 150$  days (except one outlier at 75 days), then decreases to  $-1000 \text{ km s}^{-1}$  at 150 days. In the last two epochs at which the line is detected, the blue shift has increased to  $-4000 \text{ km s}^{-1}$ . The shift of the H $\gamma$  and H $\delta$  line is always below  $|500| \text{ km s}^{-1}$  and is constant within uncertainties. It is worth noting that the velocity offsets can be affected by  $O(10^2) \text{ km s}^{-1}$  due to good observing conditions: when the seeing is better than the slit width, due to potential non perfect centering of the source in the slit, such changes can be induced. The narrow peaks of H $\alpha$  and H $\beta$  are always shifted by less than  $|500| \text{ km s}^{-1}$  and are not plotted. The shift of H $\alpha$  and H $\beta$  at each epoch is not of the same value. If we assume that the narrow H $\alpha$  and H $\beta$  originate from the host galaxy, we can expect their central wavelength to be at the laboratory values. We can use the shift measured in their central wavelength as a proxy for wavelength calibration issues or for aforementioned uncertainties due to the observing conditions. We therefore use the values of the



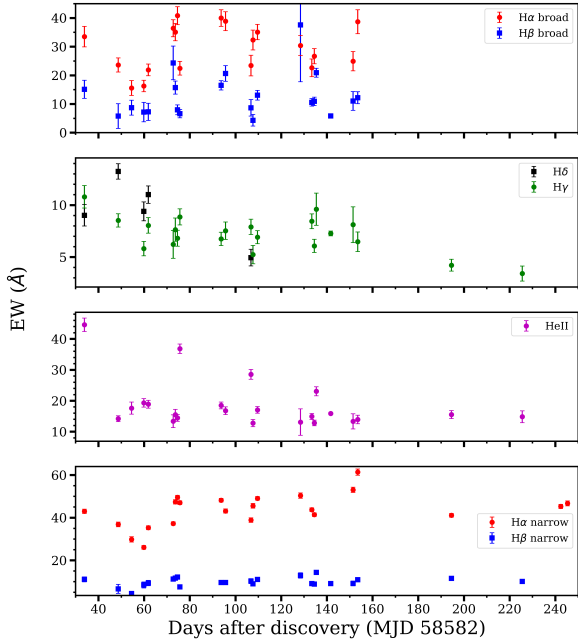


**Figure 14.** Evolution of the EW of the emission lines. From top to bottom: the broad H $\alpha$  (red circles) and H $\beta$  (blue squares), the H $\delta$  (black squares) and the H $\gamma$  (green circles), and the He II (magenta circles) emission lines caused by the TDE. Bottom panel: the narrow H $\alpha$  (red circles) and H $\beta$  (blue squares) emission lines originating in the host galaxy. Note that the redshift of AT2019dsg caused the H $\alpha$  region to coincide in wavelength with the prominent telluric feature, rendering the derived EW of H $\alpha$  uncertain. The number of days passed since the discovery of the transient is given on the X-axis.

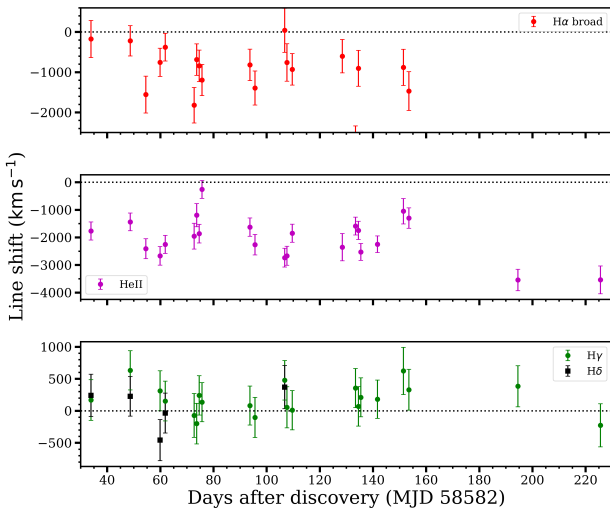


**Figure 15.** Evolution of the shift with respect to the laboratory central wavelength of the emission lines. From top to bottom: the broad H $\alpha$  (red circles), the He II (magenta circles), the H $\delta$  (black squares), and H $\gamma$  (green circles) emission lines caused by the TDE. The central wavelength of the broad H $\beta$  component was fixed during the fitting process and is not shown (see text). On the horizontal axis, the number of days passed since the discovery of the transient. Negative values indicate a blue-shift with respect to the rest frame wavelength.

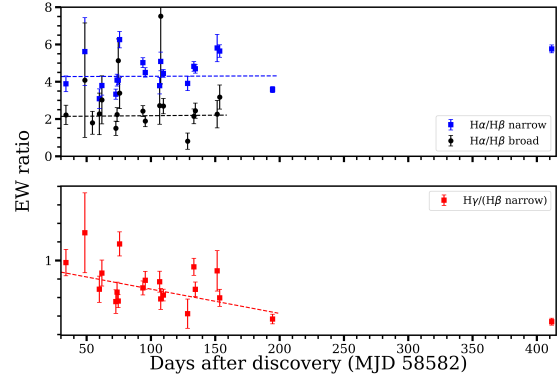


**Figure 16.** Ratio of the EW of Balmer lines. Top panel: narrow H $\alpha$ /H $\beta$  in blue squares and broad H $\alpha$ /H $\beta$  in black squares, both fitted with a straight line. The changes in the ratio between the narrow peaks are due to changes in the telluric absorption. Bottom panel: the ratio of the EW of the H $\gamma$  and the narrow H $\beta$  emission line. On the X-axis, the number of days since the discovery of the transient.

shift calculated for the narrow peak of H $\alpha$  and H $\beta$  to estimate an additional uncertainty that is reflected in the error bars of Fig. 15.

We plot the flux ratio of the Balmer lines in Fig. 16 and we fit the data with a straight line. The ratio of the narrow peaks of H $\alpha$  and H $\beta$  shows a slight increase over time. During the first  $\sim 200$  days of observations, it remains almost constant at an average value of 4.5, to then increase to 5.8. The reduced  $\chi^2$  of the fit is bad, with a value of 6.4. The ratio of the broad bases of H $\alpha$  and H $\beta$  remains constant within uncertainties at an average value of 2.4 (reduced  $\chi^2=1.9$ ). The ratio between H $\gamma$  and the narrow peak of H $\beta$  decreases from 1 to 0.3, which is also the value at the last epoch. The fit with a straight line to the data of the first  $\sim 200$  days of observations has a reduced  $\chi^2$  of 1.8.

### 3.5.4 UVES spectrum

It is interesting to consider the UVES spectrum by itself, given its higher resolution. In Fig. 17 we show the H $\beta$  region of the spectrum (H $\alpha$  is strongly affected by the telluric absorption, while the other emission lines are not strong enough with respect to the continuum, which is very noisy). The emission line in the UVES spectrum has a more box-like shape, instead of the Gaussian shape used to fit for lower resolution spectra. The line also shows evidence for structure on top. We fit this line both with a single Gaussian curve (in red in the plot), mimicking the fit of the other spectra, and with a "generalised" Gaussian (in blue):  $f(x) = a \cdot \exp\left[-\left(\frac{x-c}{2\sigma}\right)^n\right]$  with  $n > 2$  to get a flat top ( $n \approx 5$  from our fit). While the errors on the spectrum are too large to compare the reduced  $\chi^2$  and assess the goodness of fit, visually the flat-top Gaussian describes the wings of the line better. On top of this, looking at the residuals, we can see that in the case of the "regular" Gaussian fit (bottom panel of Fig. 17, in red) there are small trends in the wings of the line (4840–45 and 4862–68 Å), with respect to the flat-top Gaussian fit.

The difference between the shape of the H $\beta$  line in the UVES spectrum and in the other spectra can be accounted for by considering the different resolution. We rebin this spectrum, artificially lowering the resolution, to match the ACAM spectrum taken on 2019 July 11, which is the closest in time. The resulting spectrum is visually very similar to the ACAM one. We then fit the rebinned

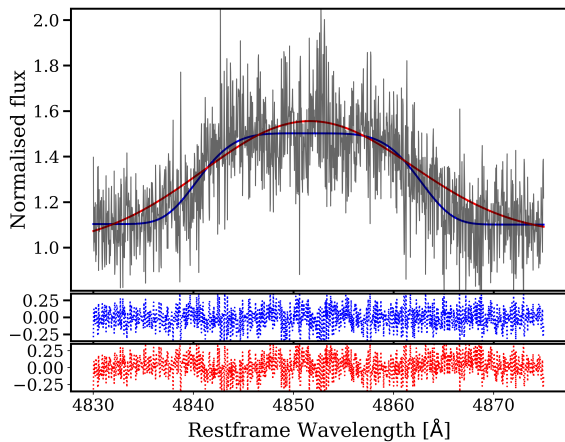


**Figure 17.**  $H\beta$  region of the UVES spectrum with two different fits: in red, the fit with a Gaussian curve, similar to the function used in the other spectra and in blue, the fit using a flat-top Gaussian. The two bottom panels are the residuals of the two fit, the top one for the flat-top Gaussian fit and the bottom one for the Gaussian fit.

UVES spectrum with the line structure used for the other spectra (of which an example is shown in Fig. 9) and we obtain line parameters within uncertainties of the ones derived from the July 11 ACAM spectrum. Notably, the broad base of  $H\beta$  and the  $He\ II$  were difficult to constrain on the unbinned UVES spectrum, probably due to the low SNR in the continuum. The complex structure at the top of the emission line is consistent with that seen in the X-shooter (Fig. 11) and ISIS spectra.

#### 4 DISCUSSION

Before discussing the interpretation of the results of our observations and analysis, we summarise the main results.

The transient is bright in X-rays, UV, optical and radio. The X-ray light curve decays very quickly and the transient becomes undetected 125 days after discovery (2019 Apr 09, MJD 58 582), while the low-frequency radio luminosity is seen to be increasing steadily. The optical spectra show a blue continuum that decays over the first 60 days of our observations. In addition, multiple broad emission lines are detected. After subtracting the stellar component of the host galaxy light, the spectra show Balmer ( $H\alpha$  through  $H\delta$ ) and  $He\ II$  4686 Å emission lines. The  $[O\ III]$  and  $[S\ II]$  doublets (4959, 5007 and 6716, 6731 Å, respectively) are also detected in emission. The  $H\alpha$  and  $H\beta$  emission lines show two components: a narrow peak and a broad base. We consider the broad base of  $H\alpha$  and  $H\beta$ , as well as the  $He\ II$  line to originate from the TDE, while the narrow emission lines as due to emission from the host galaxy. However, we do consider the narrow  $Fe\ II$  emission lines appearing 200 days after discovery in the optical spectra to be caused by the TDE. In a late time host galaxy spectrum, the broad bases of  $H\alpha$  and  $H\beta$ , the  $He\ II$  and the  $Fe\ II$  lines are no longer detected. Our medium/high resolution spectra show absorption lines superimposed on some emission lines and some emission lines show a deviation from a Gaussian profile.

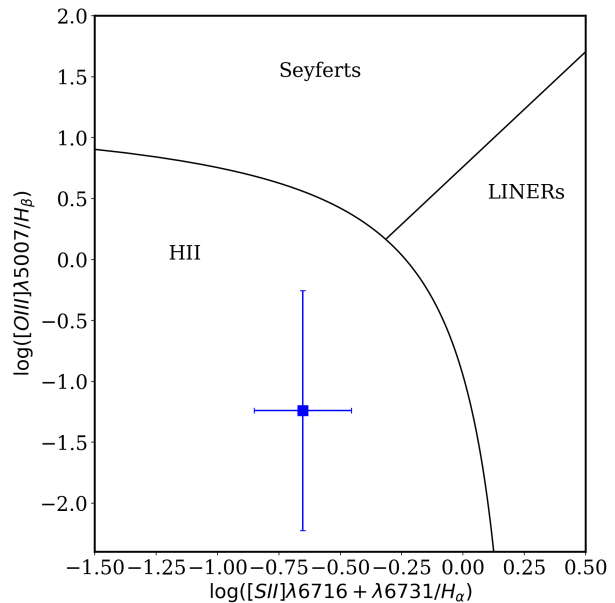


**Figure 18.** Position of the persistent narrow emission lines in the host galaxy spectrum of AT 2019dsg on a BPT diagram. The spectrum used was the late time TNG spectrum at 411 days, when no broad components to the Balmer lines could be detected. The lines separating the different regions come from Kewley et al. (2001).

#### 4.1 Constraints on the presence of an AGN

The persistence of the Balmer lines in our late time spectra, especially the narrow  $H\alpha$  and  $H\beta$  peaks, the small offset and FWHM of these lines, coupled with the apparent absence of line evolution, indicate that those narrow emission lines do not originate in the transient event, but rather in a weak AGN or are caused by star-forming activity. In order to assess the underlying ionising mechanism for these narrow emission lines we plot the position of the source on a Baldwin, Phillips & Terlevich (BPT) diagram (Baldwin et al. 1981) in Fig. 18. Due to the presence of the telluric absorption on top of the  $H\alpha$  and  $[N\ II]$  doublet lines we were not able to constrain the presence of the latter. Therefore, we are limited in the number of BPT diagrams we can use. For the BPT diagram, we use the values of the line parameters calculated from the last spectrum available, 411 days after discovery. The source falls in the  $H\ II$  region of the diagram, indicating that star formation is responsible for these narrow emission lines. In addition, the mid-infrared color from the Wide-field Infrared Survey Explorer (WISE), at  $W1-W2=-0.05$ , is lower than the threshold presented in Stern et al. (2012) for AGNs, also suggesting that the SMBH was not active prior to the TDE.

van Velzen et al. (2020) mention that the host galaxy falls in the green valley when plotting the intrinsic  $u-r$  color vs. the host galaxy mass, a region that also hosts post starburst galaxies. The narrow  $H\alpha$  and  $H\beta$  lines have a FWHM above  $1000\ km\ s^{-1}$ , which is higher than expected from an AGN narrow line region. Similarly, such a FWHM is high for most starburst galaxies, although such values have been observed in some (ultra) luminous infra-red galaxies (Arribas et al. 2014). Considering all the evidence, we exclude an AGN as the source of the narrow emission lines and favor an origin in star formation.

## 4.2 Host galaxy star light subtraction and N Bowen fluorescence lines

After we corrected the observed spectra for the contribution of the host stellar light, we do not detect the N lines associated with the Bowen fluorescence lines in any of the spectra of our follow-up campaign. We carefully inspected the spectra of AT2019dsg to investigate whether the Bowen blend is present or not. As an example we plot the line fit to the H $\delta$  to H $\beta$  region of the EFOSC2 spectrum of 2019 June 08 before the host galaxy star light is subtracted in Fig. 19. The spectrum shows an emission line at  $\sim 4050$  Å and an additional broad component between H $\gamma$  and He II. These lines have been associated with N III lines due to the Bowen fluorescence mechanism (Bowen 1934, 1935): the line at 4050 Å as the blend of two N III lines (at 4097 and 4104 Å, shifted by  $\sim 50$  Å or 3700 km s $^{-1}$ ), while the broad component at 4500 Å can be considered as a blend of many lines (see Steeghs & Casares 2002 for a list of Bowen fluorescence lines at these wavelengths). These emission lines were also identified in van Velzen et al. (2020), leading to the classification of AT2019dsg as a "TDE-Bowen". However, after the host galaxy subtraction process, both of these emission features are not detected in the spectra (see e.g., Fig. 9).

Emission lines due to the Bowen fluorescence have previously been identified in other TDEs: iPTF15af (Blagorodnova et al. 2019), AT2018dyb (Leloudas et al. 2019), ASASSN-14li (Holoien et al. 2016; Prieto et al. 2016), iPTF16fnl (Onori et al. 2019) and AT2019qiz (Nicholl et al. 2020). iPTF15af and AT2018dyb were found in non-active galaxies, while the host galaxies of iPTF16fnl, ASASSN-14li, and AT2019qiz may harbour an AGN. For iPTF15af, iPTF16fnl and AT2019qiz host galaxy subtraction was performed on the spectra, while for AT2018dyb and ASASSN-14li this was not the case (the lines were very strong in these events). The subtraction for iPTF15af was performed by fitting a late time spectrum to the source spectrum. In the case of AT2019qiz, the host subtraction was performed by creating a synthetic host galaxy spectrum using stellar population synthesis models and subtracting it from the source spectrum (this, similarly to our case, removes the stellar contribution). Finally, for iPTF16fnl, a method similar to ours was employed. For the low resolution spectra, they used PPF to scale a late time host galaxy spectrum to the source spectra to subtract it, while for their X-shooter spectra, they employed the PHOENIX library to create a synthetic host spectrum.

As a check on our host star light subtraction procedure, we also perform the subtraction of the host galaxy stellar component using the late-time TNG spectrum (411 days after the discovery of the transient) to build our synthetic host spectrum. For this spectrum, we use the MILES library (Sánchez-Blázquez et al. 2006; Falcón-Barroso et al. 2011), which consists of  $\sim 1000$  stellar spectra covering the 3525 – 7500 Å wavelength range with a resolution of 2.5 Å. Using PPF we first build the synthetic host spectrum and then we scale it to each spectrum of our follow-up campaign and subtract it. The scaling is necessary to account for variable slit losses in the data taking and for the different resolution of the detectors. In Fig. 20, we show the blue part of the observed late-time TNG spectrum, the best-fit results of the PPF procedure, i.e., the synthetic host galaxy stellar light, and the residuals. The regions with relevant emission lines, including the wavelength range associated with potential N III Bowen fluorescence features are excluded from the fit. The results of the spectral analysis on these newly subtracted spectra (including the disappearance of the N III lines and the results of the line fit) were consistent within errors with the results presented in Sec. 3.5. It is interesting to compare our AT2019dsg

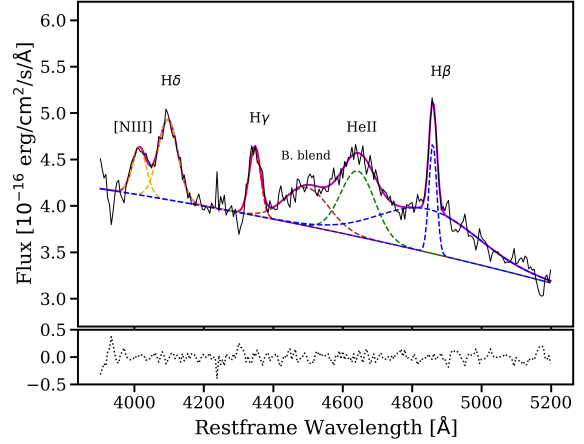


**Figure 19.** Example of a fit to the emission lines in the H $\beta$  region of the EFOSC2 spectrum taken on 2019 June 08 (60 days after discovery), before performing the host galaxy subtraction. With B. blend we indicate the blend of unresolved lines previously associated with Bowen fluorescence. In the bottom panel, the residuals of the fit are shown.

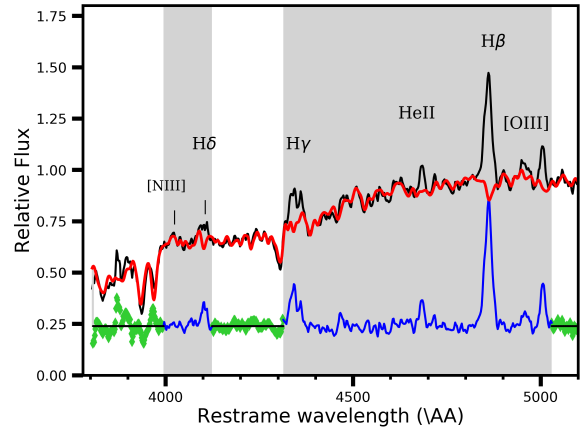


**Figure 20.** Zoom in of the H $\delta$  - H $\beta$  region on the late time TNG spectrum (+411 days). In black, the source spectrum; in red, the convolved stellar library (the PPF best-fit host galaxy synthetic spectrum); in green and blue, the subtracted spectrum. The grey vertical bands indicate the regions of the spectrum excluded from the fit. The H $\delta$  - H $\beta$  region is almost completely masked during the fit, while the rest of the spectrum, except for the H $\alpha$  line, is considered for the template fitting.

results with those of iPTF16fnl obtained by Onori et al. (2019): the spectrum used for the host subtraction in iPTF16fnl also contained a weak N III 4100 Å host galaxy line, but nevertheless the Bowen line was clearly present in the subtracted spectra (see fig. 6 of Onori et al. 2019). In all subtracted spectra, iPTF16fnl clearly shows N lines both at 4100 Å and at 4640 Å, also in the X-shooter spectra, on which the host-subtraction procedure was identical to ours. Clearly, the host stellar light subtraction procedure is not responsible for the non-detection of the N Bowen lines in AT2019dsg.

We therefore associate the presence of these emission lines in our unsubtracted spectra with spectral features originating in the host galaxy. In our synthetic spectrum (in red in Fig. 20) the area between H $\delta$  and H $\beta$  is similar to the spectrum of a green valley



galaxy (see fig. 9 of Pan et al. 2013 for an example of a green valley spectrum). That green valley galaxy spectrum clearly shows a feature at  $\sim 4020 \text{ \AA}$  that matches the one observed in our unsubtracted spectra. In addition, the host galaxy spectrum shows a bump in the continuum around  $4500 \text{ \AA}$  which when left unsubtracted can explain the erroneous identification of this feature as a blend of Bowen lines caused by TDE emission.

### 4.3 Radio emission from AT 2019dsg

In discussing the radio properties of AT 2019dsg, we also consider the radio data first published in Stein et al. (2020) (also plotted in Fig. 3). The first radio observations of AT 2019dsg started 42 days after discovery, at which time AT 2019dsg was already detectable at frequencies  $\nu \gtrsim 3 \text{ GHz}$  (Fig. 3) and showed an inverted spectrum (the higher the observing frequency, the higher the observed flux density), indicating that the radio emission was in its optically thick phase at all observed frequencies. Over time the radio emission continued to grow at all frequencies, and around day 70 AT 2019dsg started to enter its optically thin phase at frequencies  $\gtrsim 15 \text{ GHz}$ . Correspondingly, the peak frequency of AT 2019dsg started to shift progressively towards smaller values, and by day  $\sim 180$  AT 2019dsg had reached its optically thin phase also at  $\sim 6 \text{ GHz}$ . Our e-MERLIN monitoring shows, however, that the radio emission at  $5.1 \text{ GHz}$  is still rising to its maximum at  $\sim 180$  days, indicating that the TDE had not yet entered the optically thin regime at frequencies  $\lesssim 5.1 \text{ GHz}$  at that time. This result is in agreement with the value of  $\nu_{\text{peak}} = 5.4 \pm 0.1 \text{ GHz}$  at  $t = 178 \text{ d}$  reported by Stein et al. (2020). The overall radio behaviour is consistent with the evolution of gas emitting synchrotron radiation, the emission at the lower frequencies is self-absorbed. This has also been seen in other TDEs with radio emission, including both TDEs that showed a relativistic jet (e.g., Arp 299B-AT1 Mattila et al. 2018), and those where the relativistic/sub-relativistic nature of the outflow is less clear (e.g., van Velzen et al. 2016; Alexander et al. 2016). Stein et al. (2020) have modelled the radio emission of AT 2019dsg as a synchrotron self-absorbed sub-relativistic outflow that has a continuous injection of fresh relativistic electrons from a central engine. But we note that in the case of the TDE Arp 299-B AT1, Mattila et al. (2018) modelled the radio emission with a relativistic jet whose initial population of electrons are continuously re-accelerated. Stein et al. (2020) find that the expansion of the TDE proceeds with a constant speed for the first three epochs, until day 120, and then suffers an increase in expansion speed at the latest epoch. However, we note that this explanation is not unique and probably model dependent, as the outflow radius is not measured directly. A relativistic jet with a fast core and a slow sheath seems to be able to account for an almost constant expansion (of the fast jet) as well (Mimica et al. 2015), although we defer detailed radio modelling to future work. Similarly, the increase of the expansion speed seen around day 180 for AT 2019dsg can also be explained by a relativistic jet that encounters a medium with a steep density profile, as found by Mattila et al. (2018) for Arp 299B-AT1. The  $5.0 \text{ GHz}$  radio emission of Arp 299-B AT1 peaked at substantially later epochs, more than  $\sim 1000$  days after the event. In contrast, ASASSN-14li (e.g., Bright et al. (2018)) and AT2017gbl (Kool et al. 2020), showed their  $5.0 \text{ GHz}$  emission peaking around 150 days. At the end of our follow-up, the  $5.0 \text{ GHz}$  emission from AT 2019dsg has still not reached its peak. We stress that a comparison of phases across different TDEs is not straightforward, as we define time=0 as the discovery of the transient, and not as some moment related to the physics of the event.

### 4.4 X-rays: disc cooling?

The X-ray luminosity decays very quickly, decreasing by a factor  $\sim 100$  in roughly 60 days, and becomes undetected 125 days after discovery, although we lack deep late-time *Chandra* or *XMM-Newton* observations (cf. Jonker et al. 2020). To explain such a dramatic decrease, we can invoke several possible mechanisms that can work alone or in conjunction, such as: (i) an increase in absorption in our line of sight to the X-ray emitting region or (ii) cooling of the disc that causes the emission to shift out of the X-ray band, caused by either a general decrease in mass accretion rate, reducing the energy output, or by an increase in the amount of ionized material causing the X-ray photosphere to move out with time.

The observed cooling of the black body temperature in X-ray spectral fits to the NICER data (Fig. 6) suggest that the first mechanism is not at play, as it would make the observed spectrum harder with time. Furthermore, following the TDE unification idea (Dai et al. 2018) the cooling X-ray disc seems to suggest that we are observing the system relatively pole-on. The second mechanism mentioned above could be at play. We see a decrease in temperature over the first 60 days after discovery of the transient. If this cooling continued, the emission shifts out of the X-ray pass band. Indeed, in the last Swift detection (125 days after discovery), the photons were all detected below  $0.5 \text{ keV}$ . The X-ray luminosity seems to follow the Stefan-Boltzmann law (Fig. 7), meaning that the emission from the disc is consistent with a thermal nature.

What is causing this cooling is unclear: potentially the mass accretion rate is dropping, or alternatively, the photosphere is moving out, due to increased presence of ionized material. The black body radius obtained from the modeling of the X-ray spectrum using a black body model,  $R = 3.4_{-0.9}^{+1.5} \times 10^{11} \text{ cm}$  is smaller than the Schwarzschild radius of a  $(5.4 \pm 3.2) \times 10^6 M_{\odot}$  BH,  $R_S = (1.6 \pm 0.9) \times 10^{13} \text{ cm}$ . While a more edge-on view of the accretion disc could cause the observed emitting region to appear smaller another possible explanation involves the properties of the atmosphere above the accretion disc. Due to a rapid decrease of the opacity with X-ray photon energy due to light element free-free, bound-free, and bound-bound transitions, higher energy X-ray photons are coming from deeper, hotter layers (see for instance the explanation in Zavlin & Pavlov 2002). This effect is seen in quiescent neutron stars (NS), where the presence of an atmosphere causes the emitting radius to be underestimated if modeled with a simple black body (see Kaspi et al. 2010, for a review). It is worth noting that finding black body radii too small for the BH masses is not uncommon in TDEs (e.g., Wevers et al. 2019a).

To better understand the driver behind the decay in X-ray luminosity, we also checked the He II  $4686 \text{ \AA}$  line EW. The He II  $4686 \text{ \AA}$  line is known to be created by photo-ionisation due to (soft) X-ray photons, exhibiting photon-counting properties with a rough correspondence of 1 He II photon emitted for each 0.3-10 keV X-ray photon (Pakull & Angebault 1986; Schaerer, D. et al. 2019). If we compare the photon emission in the X-rays with the He II line EW, we see that the rate of photons emitted in the X-rays is above the amount necessary to explain the detected He II emission line at all epochs where we have data, by a factor of  $\sim 100$  at the beginning reducing to a factor  $\sim 2$  at the last X-ray detection (125 days after discovery). The He II luminosity does not trace the initial dramatic decrease present in the X-ray light curve. Instead, its EW only decreases by a factor  $\sim 4$  between 30 and 50 days after the discovery date. This could suggest that the region responsible for the He II emission is (partially) shielded from our line of sight, i.e., the X-ray emission is not "seen" by all material surrounding the black hole.

There is suggestive evidence for short term variability in the Swift X-ray data. Other TDEs have shown similar X-ray *flaring* activity (e.g., AT2019ehz, van Velzen et al. 2020 and SDSS J1201, Saxton et al. 2012). This behaviour can for instance be explained by a clumpy outflow. Another cause for short-term X-ray variability could be precession of the accretion disc. In such a scenario, when viewed under a large inclination, the disc can intermittently obscure the inner X-ray emitting region. The inclination angle changes due to precession creating the modulation of the light curve on the precession timescale (Franchini et al. 2016; Wen et al. 2020). In our case, we favour a more polar line of sight to the system and therefore, we deem the precession scenario as an explanation for the X-ray variability in AT2019dsg less likely. To explain the variability observed in the Swift lightcurve (Fig. 5), we could invoke the debris streams caused by the initial disruption of the star. As explored in more detail in Sec. 4.7, when the star is disrupted, the debris will form self gravitating streams (Guillochon et al. 2014). If some of these streams are deflected to high enough angles by nodal precession, they could (occasionally) intercept our line of sight to the inner accretion disc, where the X-rays are produced. The variability of the EW of He II (Fig. 14) could be reflecting the variability observed in the Swift X-ray light curve.

At late times (more than 200 days), we start seeing low ionisation Fe II emission lines in the spectra. These lines are produced in an optically thick, high density medium, ionised by X-ray radiation. Low ionisation Fe II lines have already been observed in TDEs, as reported in Wevers et al. (2019b), where the authors compare the emergence of these lines to the case of Cataclysmic Variables, where these lines are thought to originate from the surface of the accretion disc. AT2019dsg is the third UV/optical detected TDE that show these low ionisation, optical Fe II emission lines, the other two being AT2018fyk and ASASSN-15oi (Wevers et al. 2019b). We identify emission from multiplets 37, 38, 42 and 49, which are some of the strongest features also observed in some AGN. These three Fe-strong TDEs show several similarities in their observed properties. Similar to AT2018fyk and ASASSN-15oi, AT2019dsg produced observable X-ray emission (although, note that at the epochs at which we detect the Fe II lines we do not have X-ray data). The Fe lines observed are much narrower than the other TDE lines. As explored below (see Section 4.6), following Roth & Kasen (2018a), we hypothesise that in AT2019dsg the broad lines due to the TDE (He II, H $\alpha$  and H $\beta$ ) are created in an expanding photosphere that causes the shift of the line centroid and the large FWHM. Therefore, we assume that the Fe lines do not originate in this expanding photosphere, but rather in optically thick clumps of gas. This gas is either pre-existing but only irradiated by X-rays at later times for instance due to disc slimming (Wen et al. 2020) or low-velocity condensations of earlier outflowing material. While the late-time presence of the Fe lines reinforces the idea that there is still X-ray emission, their ionisation potential is only a few eV, so that even a "cool" disc could be sufficient to ionise them.

#### 4.5 N Bowen fluorescence lines

Besides showing late-time Fe emission lines, AT2018fyk, ASASSN-15oi, and AT2019dsg have another common characteristic: their spectra show no evidence for N III Bowen fluorescence emission. On the other hand, emission features near 3760 Å do appear in all three sources (see e.g., the UVES and ISIS spectra in Fig. 1).

The wavelengths of the 3760 Å features coincide with a group of transitions that can be directly linked to both excited states

pumped by the primary Bowen fluorescence process of Oxygen (Bowen 1934). An alternative explanation for these features could be Fe II emission lines from multiplets 120 and 29 (Netzer & Wills 1983), which can be particularly strong due to Fe II self-fluorescence (i.e., wavelengths coincidences between Fe II transitions). However, due to the presence of several transient forbidden transitions of O III (including  $\lambda$ 4363, 4960) in the Fe-strong TDEs, we prefer the former explanation.

Why do we observe Bowen O III lines but not the typical N III lines in Fe-strong TDEs? The Bowen fluorescence mechanism is based on a chain of photo-(de)excitations that arise from a strong X-ray ionising source exciting He II Ly- $\alpha$  photons and a dense medium. The primary fluorescence occurs through Oxygen, whose transitions in turn have resonances that can pump N atoms to excited states. In particular, the O III cascade produces the  $2p3s\ ^3P^0$  state through de-excitations including (among others) the 3760 Å transitions. This unstable state subsequently decays through UV resonance lines ( $\lambda$  374.432, 374.162 Å) with N III. This results in N III emission near the 4640 Å complex that is the hallmark of Bowen fluorescence, observed in X-ray binaries (McClintock et al. 1975), novae (Selvelli et al. 2007), planetary nebulae, QSOs (Weymann & Williams 1969) and TDEs (Blagorodnova et al. 2019; Leloudas et al. 2019; Onori et al. 2019).

If resonant line fluorescence is efficient, one would then expect to see N III 4640 Å emission whenever the O III 3760 Å feature is present. However, this does not appear to be the case for Fe-strong TDEs. One straightforward explanation is that the N III 4640 Å emission feature is *hidden* in the Fe II complex. However, the majority of TDEs with Bowen lines have N III 4640 Å emission line fluxes that exceed the O III 3760 Å fluxes (Leloudas et al. 2019). In addition, the 4640 Å feature is clearly visible even next to the dominant He II 4686 Å line. This suggests that the line strength of N III 4640 Å is much lower in Fe-strong TDEs. In other words, the resonant line fluorescence of N III is much less efficient.

Probably the absence of significant N III emission reflects different physical conditions along our line of sight in N- and Fe-strong TDEs. In particular, Selvelli et al. (2007) argued that the key to pumping N III resonance lines is multiple scatterings in an optically thick medium. In optically thin conditions, the probability that an O III resonance photon will directly excite the parent level that results in N III 4640 Å emission is very low. However, if the medium is optically thick, multiple scatterings of the O III photon results in a very high probability of ultimately triggering the N III emission. A more detailed, quantitative analysis to infer the physical properties of the gas will require high SNR spectroscopy of the Bowen lines, including those in the UV part of the spectrum which we are lacking for AT2019dsg, combined with radiative transfer modelling.

#### 4.6 Broad optical emission lines

It is interesting to consider the evolution of the parameters of the (broad) emission lines detected in AT2019dsg. The EW and the FWHM of the H $\gamma$  line both show a decrease (by a factor  $\sim 2$ ) between 30 and 70 days after discovery, a timescale that is similar to the one over which the blue continuum of the optical spectra decays. More interestingly, the EW of the H $\gamma$  line shows a gradual decrease over the whole period of our follow-up campaign. Potentially, there might be two components to that emission line (similarly to H $\alpha$  and H $\beta$  case): one from the host galaxy and another one from the TDE. However, in the case of the H $\gamma$ , we are not able to separate these two components in a narrow and a broad line. The decrease of the EW can be explained by the decay of the broad component arising

from the TDE. From 190 days onwards, we are probably detecting only the contribution from the host galaxy narrow emission line: the value of the EW is almost a factor 2 lower than the previous data point and does not change any further (see also Tab. B2). The broad component of H $\alpha$  and H $\beta$  also is no longer detected at these epochs. If the central wavelength is dominated by the narrow line component originating in the host galaxy, this would also explain the low shift of the central wavelength detected in this line (and in H $\delta$  in the few epochs in which it is constrained). Finally, also the decrease of the ratio between the EW of the H $\gamma$  and that of the narrow H $\beta$  (Fig. 16) could be explained by the H $\gamma$  having these two components.

The evolution of the He II is also interesting: it is the only line to show a consistent blueshift with respect to the restframe wavelength, and this blueshift is increasing in the last two epochs. The amplitude of this blueshift is in line with the velocity of the radio outflow derived in Stein et al. (2020), which is also increasing around 170 days after discovery. The FWHM of the He II also increases at the same time. This could mean that the He II line originates in expanding gas that traces the outflow that could be responsible for the radio emission as well. Its FWHM is then partly determined by electron scattering (Roth & Kasen 2018b) and partly by differences in the outflow velocities projected onto our line of sight of the He II emitting gas. The broad components of H $\alpha$  and H $\beta$  have FWHMs with of similar or greater values compared to He II. They could also originate from an expanding shell of gas. Also the velocity shift of the broad base of H $\alpha$  has a value similar to the one of He II. Unfortunately, the broad H $\alpha$  and H $\beta$  were not detected at the last two epochs when the blueshift of the He II line increases. The scenario of expanding material, where X-ray radiation is reprocessed and the broad optical lines are emitted, is similar to the one discussed in Nicholl et al. (2020) for the TDE AT 2019qiz.

#### 4.7 High resolution spectroscopy and absorption lines

In our follow-up campaign of AT 2019dsg we obtained two medium resolution spectra (ISIS and X-shooter) and one high resolution spectrum (UVES). In these spectra, we see evidence for absorption lines superimposed on the broad emission lines: in both the X-shooter (Fig. 11) and ISIS (Fig. 12) spectra, the H $\gamma$  and He II lines show absorption lines. The UVES spectrum (Fig. 17) also provides suggestive evidence for the presence of several absorption lines superimposed on the H $\beta$  line. Unfortunately, the SNR of the UVES spectrum is too low to establish the presence of these potential absorption lines beyond doubt. The spectrum does show evidence that the overall line shape may deviate from a simple Gaussian profile. The H $\beta$  line shows a flat top. Deviations from a Gaussian profile of the broad emission lines of a TDE have been seen before in the literature, with lines showing double peaks and box-shaped profiles (Short et al. 2020).

We thoroughly checked our synthetic host spectrum for features that could artificially create the absorption lines detected in the H $\gamma$  and He II lines, during the host-subtraction procedure, but found none. The absorption lines could be due to the host galaxy. On one hand, if this were the case, we would expect the line parameters to not change between the two spectra, especially since they are separated by just 7 days (the line parameters are reported in Tab. 4). Indeed, the line parameters are consistent to within uncertainties. On the other hand, these lines are present in the spectra after we removed the stellar component, disfavoured such an origin. We check for absorption from diffuse atmospheric bands (DIBs), finding

that only the absorption feature in He II at 4660 Å could potentially be explained by the DIB at 4659.8 Å (Hobbs et al. 2008).

When a star is disrupted, the debris may form strongly self-gravitating streams (Guillochon et al. 2014). What we could be seeing is absorption lines caused by such streams, where the different orbital motions and projected velocities of these different streams cause the variation of the width of the lines. To have this, we would need some of the self-gravitating streams to be deflected by large angles, while the bulk of the disrupted material circularises into an accretion disc, as we deem it likely that the disc is observed under a low inclination angle. Detecting these streams could be an indicator of the BH spin: in fact, to produce the detected absorption lines, the streams have to be somewhat long-lived (in our case, for at least 140–150 days). This happens if the streams do not self-intersect during their orbital motion. As suggested in Guillochon & Ramirez-Ruiz (2015), the relativistic precession induced by the BH spin can deflect the streams from the original orbital plane, thus avoiding their intersection. This effect is more pronounced for retrograde orbits (Hayasaki et al. 2016) than for prograde ones (Liptai et al. 2019). It is important to note that in Leloudas et al. (2019), a search for such absorption features in their UVES spectra is presented, without finding any absorption line due to the TDE. Overall, it is unclear if such streams can be present while at the same time active accretion is ongoing.

TDEs are geometrically complicated phenomena, with streams of debris self-intersecting, outflows, an accretion disc which is not expected to have a simple and symmetric geometry - especially at the beginning of the outburst - and it is only natural for this complex environment to be reflected in the spectral properties. In the future, employing high resolution spectrographs and developing physical models that account for the fine structure observed could be paramount to obtain a more thorough picture of the dynamics of the debris stream, the eventual formation of the accretion disc and to infer the spin of the BH.

## 5 SUMMARY

We present results of a spectroscopic monitoring campaign of the tidal disruption event AT2019dsg. We perform a detailed analysis of the emission line content and evolution at optical wavelengths, using 26 spectra covering 34 to 411 days after discovery. Combining these results with other multi-wavelength information, including radio interferometric observations and X-ray and UV measurements, we attempt to explain the multi-wavelength observed properties and their evolution in a coherent manner.

- The TDE is X-ray bright, but the X-ray luminosity rapidly decays and becomes undetectable in less than 200 days. This rapid decline can be explained with a cooling disc.
- In line with Stein et al. (2020) we suggest that an outflow is powered by the accretion flow and the outflow is responsible for the optical (line) emission. The emission lines, particularly He II, trace the outflow velocity (which, as modeled in Stein et al. 2020, increases between 120 and 180 days after discovery). We therefore propose that the emission lines are formed in this expanding medium.
- Our e-MERLIN radio observations show that the emission is still increasing at 5.1 GHz, in contrast with radio observations at higher frequencies, which show a clear decreasing trend. This indicates that the TDE is still optically thick at  $t \sim 200$  d for  $\nu \lesssim 5.1$  GHz. While Stein et al. (2020) interpreted their radio observations as being due to a sub-relativistic outflow, we warn that a relativistic



jet with a fast core and a slow sheath could possibly also explain the radio observations (see, e.g., [Mimica et al. 2015](#)) and, advocating a change in the density profile, the apparent increase in the expansion speed around day 180.

- At later times, more than 200 days after discovery, low ionisation Fe emission lines appear. We do not have X-ray data at these epochs, but the presence of the Fe lines indicates the continued presence of an ionising continuum source.

- We show that after carefully subtracting the host galaxy light, the features previously identified as N III Bowen fluorescence lines by [van Velzen et al. \(2020\)](#) disappear. This underlines the importance of performing host galaxy subtraction for the spectral study of TDEs.

- We discuss the similarities between the Fe-strong TDEs in terms of the presence/absence of Fe and N Bowen fluorescence lines.

- In our medium/high resolution spectra, we see absorption lines that could be due to the self-gravitating debris streams, caused by the disruption of the star, intercepting our line of sight. High resolution spectroscopy may play a big role in the future for understanding the dynamics of the debris stream in TDEs.

## ACKNOWLEDGEMENTS

GC and PGJ acknowledge support from European Research Council (ERC) Consolidator Grant 647208. TW is funded by ERC grant 320360 and by European Commission grant 730980. This research was made possible through the use of the AAVSO Photometric All-Sky Survey (APASS), funded by the Robert Martin Ayers Sciences Fund and NSF AST-1412587. We acknowledge the use of public data from the *Swift* data archive. We thank P. M. Vreeswijk for the data reduction of the UVES spectrum. This paper includes data obtained with the William Herschel Telescope (proposal IDs: W19B/P7, W19A/N3) as well as observations made with the Italian Telescopio Nazionale Galileo (TNG) operated on the island of La Palma by the Isaac Newton Group of Telescopes and the Fundación Galileo Galilei of the INAF (Istituto Nazionale di Astrofisica) at the Spanish Observatorio del Roque de los Muchachos of the Instituto de Astrofísica de Canarias. Based on observations collected at the European Organisation for Astronomical Research in the Southern Hemisphere under ESO programmes 1103.D-0328 "advanced Public ESO Spectroscopic Survey for Transient Objects" (ePESSTO+). GL was supported by a research grant (19054) from VILLUM FONDEN. D.M-S. acknowledges support from the ERC under the European Union's Horizon 2020 research and innovation programme (grant agreement No. 715051; Spiders). JM acknowledges financial support from the State Agency for Research of the Spanish MCIU through the "Center of Excellence Severo Ochoa" award to the Instituto de Astrofísica de Andalucía (SEV-2017-0709) and from the grant RTI2018-096228-B-C31 (MICIU/FEDER, EU). IA is a CIFAR Azrieli Global Scholar in the Gravity and the Extreme Universe Program and acknowledges support from that program, from the European Research Council (ERC) under the European Union's Horizon 2020 research and innovation program (grant agreement number 852097), from the Israel Science Foundation (grant numbers 2108/18 and 2752/19), from the United States - Israel Binational Science Foundation (BSF), and from the Israeli Council for Higher Education Alon Fellowship. TWC acknowledges the EU Funding under Marie Skłodowska-Curie grant H2020-MSCA-IF-2018-842471. TMB was funded by the CONICYT PFCHA / DOCTORADOBECAS

CHILE/2017-72180113. MN is supported by a Royal Astronomical Society Research Fellowship.

## Data Availability

All data will be made available in a reproduction package uploaded to Zenodo.

## REFERENCES

- Alexander K. D., Berger E., Guillochon J., Zauderer B. A., Williams P. K. G., 2016, *ApJ*, **819**, L25
- Alexander K. D., van Velzen S., Horesh A., Zauderer B. A., 2020, *Space Sci. Rev.*, **216**, 81
- Arcavi I., et al., 2014, *ApJ*, **793**, 38
- Arnaud K. A., 1996, in Jacoby G. H., Barnes J., eds, *Astronomical Society of the Pacific Conference Series Vol. 101, Astronomical Data Analysis Software and Systems V*. p. 17
- Arribas S., Colina L., Bellocchi E., Maiolino R., Villar-Martín M., 2014, *A&A*, **568**, A14
- Baldwin J. A., Phillips M. M., Terlevich R., 1981, *PASP*, **93**, 5
- Ballester P., Modigliani A., Boitquin O., Cristiani S., Hanuschik R., Kaufer A., Wolf S., 2000, *The Messenger*, **101**, 31
- Blagorodnova N., et al., 2017, *ApJ*, **844**, 46
- Blagorodnova N., et al., 2019, *ApJ*, **873**, 92
- Bonnerot C., Lu W., 2019, arXiv e-prints, p. [arXiv:1906.05865](#)
- Bowen I. S., 1934, *PASP*, **46**, 146
- Bowen I. S., 1935, *ApJ*, **81**, 1
- Bright J. S., et al., 2018, *MNRAS*, **475**, 4011
- Brown T. M., et al., 2013, *PASP*, **125**, 1031
- Cappellari M., 2017, *MNRAS*, **466**, 798
- Dai L., McKinney J. C., Roth N., Ramirez-Ruiz E., Miller M. C., 2018, *ApJ*, **859**, L20
- Davenport J., de Val-Borro M., Wilkinson T. D., 2016, pydis: Possibly Useful, [doi:10.5281/zenodo.58753](#), <https://doi.org/10.5281/zenodo.58753>
- Evans C. R., Kochanek C. S., 1989, *ApJ*, **346**, L13
- Falcón-Barroso J., Sánchez-Blázquez P., Vazdekis A., Ricciardelli E., Cardiel N., Cenarro A. J., Gorgas J., Peletier R. F., 2011, *A&A*, **532**, A95
- Ferrarese L., Ford H., 2005, *Space Sci. Rev.*, **116**, 523
- Filippenko A. V., 1982, *PASP*, **94**, 715
- Franchini A., Lodato G., Facchini S., 2016, *MNRAS*, **455**, 1946
- French K. D., Arcavi I., Zabludoff A., 2016, *ApJ*, **818**, L21
- Freudling W., Romaniello M., Bramich D. M., Ballester P., Forchi V., García-Dabó C. E., Moehler S., Neuser M. J., 2013, *A&A*, **559**, A96
- Gehrels N., et al., 2004, *ApJ*, **611**, 1005
- Gendreau K. C., et al., 2016, in *Space Telescopes and Instrumentation 2016: Ultraviolet to Gamma Ray*. p. 99051H, [doi:10.1117/12.2231304](#)
- Guillochon J., Ramirez-Ruiz E., 2015, *ApJ*, **809**, 166
- Guillochon J., Manukian H., Ramirez-Ruiz E., 2014, *ApJ*, **783**, 23
- Gültekin K., et al., 2009, *ApJ*, **698**, 198
- HI4PI Collaboration et al., 2016, *A&A*, **594**, A116
- Hayasaki K., Stone N., Loeb A., 2016, *MNRAS*, **461**, 3760
- Henden A. A., 2019, *Journal of the American Association of Variable Star Observers (JAAVSO)*, **47**, 130
- Hills J. G., 1975, *Nature*, **254**, 295
- Hobbs L. M., et al., 2008, *The Astrophysical Journal*, **680**, 1256–1270
- Holoien T. W. S., et al., 2016, *MNRAS*, **455**, 2918
- Holoien T. W. S., Brown J. S., Auchettl K., Kochanek C. S., Prieto J. L., Shappee B. J., Van Saders J., 2018, *MNRAS*, **480**, 5689
- Hung T., et al., 2020, arXiv e-prints, p. [arXiv:2003.09427](#)
- Husser T. O., Wende-von Berg S., Dreizler S., Homeier D., Reiners A., Barman T., Hauschildt P. H., 2013, *A&A*, **553**, A6



- Jonker P. G., Stone N. C., Generozov A., van Velzen S., Metzger B., 2020, *ApJ*, **889**, 166
- Jordi K., Grebel E. K., Ammon K., 2006, *A&A*, **460**, 339
- Kaspi V. M., Roberts M. S. E., Harding A. K., 2010, Isolated neutron stars. p. 279
- Kausch W., et al., 2015, *A&A*, **576**, A78
- Kewley L. J., Heisler C. A., Dopita M. A., Lumsden S., 2001, *ApJS*, **132**, 37
- Komossa S., 2002, in Gilfanov M., Sunyaev R., Churazov E., eds, *Lighthouses of the Universe: The Most Luminous Celestial Objects and Their Use for Cosmology*. p. 436 ([arXiv:astro-ph/0109441](https://arxiv.org/abs/astro-ph/0109441)), [doi:10.1007/10856495\\_62](https://doi.org/10.1007/10856495_62)
- Kool E. C., et al., 2020, *MNRAS*, **498**, 2167
- Leloudas G., et al., 2016, *Nature Astronomy*, **1**, 0002
- Leloudas G., et al., 2019, arXiv e-prints,
- Liptai D., Price D. J., Mandel I., Lodato G., 2019, arXiv e-prints, [p. arXiv:1910.10154](https://arxiv.org/abs/1910.10154)
- Mattila S., et al., 2018, *Science*, **361**, 482
- McClintock J. E., Canizares C. R., Tarter C. B., 1975, *ApJ*, **198**, 641
- McConnell N. J., Ma C.-P., 2013, *ApJ*, **764**, 184
- McCully C., et al., 2018, LcoGT/Banzai: Initial Release, [doi:10.5281/zenodo.1257560](https://doi.org/10.5281/zenodo.1257560)
- McMullin J. P., Waters B., Schiebel D., Young W., Golap K., 2007, *CASA Architecture and Applications*. p. 127
- Mimica P., Giannios D., Metzger B. D., Aloy M. A., 2015, *MNRAS*, **450**, 2824
- Netzer H., Wills B. J., 1983, *ApJ*, **275**, 445
- Newville M., Stensitzki T., Allen D. B., Ingargiola A., 2014, LM-FIT: Non-Linear Least-Square Minimization and Curve-Fitting for Python, [doi:10.5281/zenodo.11813](https://doi.org/10.5281/zenodo.11813), <https://doi.org/10.5281/zenodo.11813>
- Nicholl M., et al., 2019a, *MNRAS*, **488**, 1878
- Nicholl M., et al., 2019b, *The Astronomer's Telegram*, **12752**, 1
- Nicholl M., et al., 2020, arXiv e-prints, [p. arXiv:2006.02454](https://arxiv.org/abs/2006.02454)
- Onori F., et al., 2019, *MNRAS*, **489**, 1463
- Pakull M. W., Angebault L. P., 1986, *Nature*, **322**, 511
- Pan Z., Kong X., Fan L., 2013, *ApJ*, **776**, 14
- Piran T., Svirski G., Krolik J., Cheng R. M., Shiokawa H., 2015, *ApJ*, **806**, 164
- Planck Collaboration et al., 2014, *A&A*, **571**, A16
- Prieto J. L., et al., 2016, *ApJ*, **830**, L32
- Prugniel P., Soubiran C., 2001, *A&A*, **369**, 1048
- Rees M. J., 1988, *Nature*, **333**, 523
- Roth N., Kasen D., 2018a, *ApJ*, **855**, 54
- Roth N., Kasen D., 2018b, *ApJ*, **855**, 54
- Sánchez-Blázquez P., et al., 2006, *MNRAS*, **371**, 703
- Saxton R. D., Read A. M., Esquej P., Komossa S., Dougherty S., Rodríguez-Pascual P., Barrado D., 2012, *A&A*, **541**, A106
- Schaerer, D. Fragos, T. Izotov, Y. I. 2019, *A&A*, **622**, L10
- Schawinski K., et al., 2014, *MNRAS*, **440**, 889
- Schlafly E. F., Finkbeiner D. P., 2011, *ApJ*, **737**, 103
- Selvelli P., Danziger J., Bonifacio P., 2007, *A&A*, **464**, 715
- Shiokawa H., Krolik J. H., Cheng R. M., Piran T., Noble S. C., 2015, *ApJ*, **804**, 85
- Short P., et al., 2020, *Monthly Notices of the Royal Astronomical Society*, **498**, 4119
- Smartt S. J., et al., 2015, *A&A*, **579**, A40
- Smette A., et al., 2015, *A&A*, **576**, A77
- Steehls D., Casares J., 2002, *ApJ*, **568**, 273
- Stein R., Franckowiak A., Necker J., Gezari S., Velzen S. v., 2019a, *The Astronomer's Telegram*, **13160**, 1
- Stein R., Franckowiak A., Necker J., Gezari S., van Velzen S., Ztf Collaboration Growth Collaboration 2019b, GRB Coordinates Network, **25929**, 1
- Stein R., et al., 2020, arXiv e-prints, [p. arXiv:2005.05340](https://arxiv.org/abs/2005.05340)
- Stern D., et al., 2012, *ApJ*, **753**, 30
- Stone N. C., Metzger B. D., 2016, *MNRAS*, **455**, 859
- Tody D., 1986, in Crawford D. L., ed., *Proc. SPIE Vol. 627, Instrumentation in astronomy VI*. p. 733, [doi:10.1117/12.968154](https://doi.org/10.1117/12.968154)
- Valenti S., et al., 2014, *MNRAS*, **438**, L101
- Vernet J., et al., 2011, *A&A*, **536**, A105
- Wen S., Jonker P. G., Stone N. C., Zabludoff A. I., Psaltis D., 2020, *ApJ*, **897**, 80
- Wevers T., 2020, *MNRAS*, **497**, L1
- Wevers T., van Velzen S., Jonker P. G., Stone N. C., Hung T., Onori F., Gezari S., Blagorodnova N., 2017, *MNRAS*, **471**, 1694
- Wevers T., et al., 2019a, *MNRAS*, **487**, 4136
- Wevers T., et al., 2019b, *MNRAS*, **488**, 4816
- Weymann R. J., Williams R. E., 1969, *ApJ*, **157**, 1201
- Wyryzkowski Ł., et al., 2017, *MNRAS*, **465**, L114
- Zavlin V. E., Pavlov G. G., 2002, in Becker W., Lesch H., Trümper J., eds, *Neutron Stars, Pulsars, and Supernova Remnants*. p. 263 ([arXiv:astro-ph/0206025](https://arxiv.org/abs/astro-ph/0206025))
- van Velzen S., et al., 2016, *Science*, **351**, 62
- van Velzen S., et al., 2020, arXiv e-prints, [p. arXiv:2001.01409](https://arxiv.org/abs/2001.01409)

**APPENDIX A: FLOYDS SPECTRA**

**APPENDIX B: LINE FITTING RESULTS**

**APPENDIX C: PHOTOMETRY DATA**

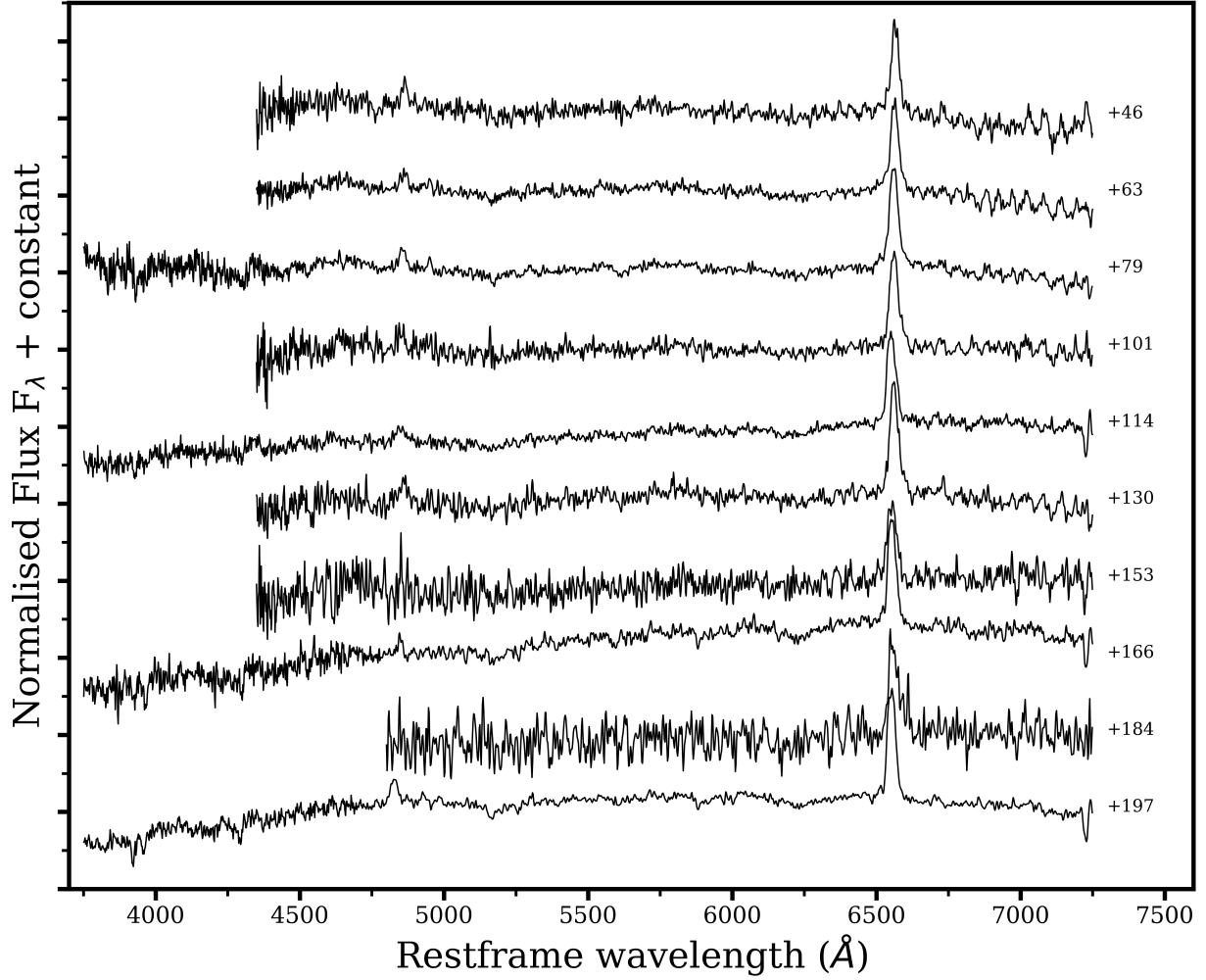


**Figure A1.** Sequence of spectra taken with the FLOYDS spectrograph. For each spectrum the phase with respect to the transient discovery date (2019 Apr 09, MJD 58582) is reported on the right. For plotting purposes, all spectra have been divided by their median value.

**Table A1.** FLOYDS spectroscopic observations

MJD <sup>(1)</sup> [days]	phase <sup>(2)</sup> [days]	UTC Date	exposure time [s]	slit [ $''$ ]
58 628.73	+46	2019 May 25	3600	2.0
58 645.65	+63	2019 Jun 11	3600	2.0
58 661.72	+79	2019 Jun 27	3600	2.0
58 683.66	+101	2019 Jul 19	3600	2.0
58 696.65	+114	2019 Aug 01	3600	2.0
58 712.49	+130	2019 Aug 17	3600	2.0
58 735.55	+153	2019 Sep 09	3600	2.0
58 748.41	+166	2019 Sep 22	3600	2.0
58 766.46	+184	2019 Oct 10	3600	2.0
58 779.35	+197	2019 Oct 23	3600	2.0

*Note.* (1) Modified Julian Day of observations; (2) calculated with respect to the discovery date MJD 58 582.

**Table B1.** FWHM of the emission lines, in  $\text{km s}^{-1}$  as measured from our spectra at epoch given by the Modified Julian Date in the first column, corrected for instrumental broadening. With  $\dots$  we indicate an epoch in which the line in question could not be fit.

MJD <sup>(1)</sup>	phase <sup>(2)</sup>	H $\delta$	H $\gamma$	He II	H $\beta$ broad	H $\alpha$ broad	H $\beta$ narrow	H $\alpha$ narrow
58 616.36	+34	3880 $\pm$ 340	3560 $\pm$ 280	9850 $\pm$ 370	5800 $\pm$ 740	11970 $\pm$ 1010	1110 $\pm$ 110	920 $\pm$ 60
58 631.13	+49	4630 $\pm$ 200	3020 $\pm$ 170	5790 $\pm$ 290	2720 $\pm$ 740	8840 $\pm$ 670	1010 $\pm$ 220	1020 $\pm$ 70
58 638.28	+55	$\dots$	$\dots$	7610 $\pm$ 660	4310 $\pm$ 760	7540 $\pm$ 880	1180 $\pm$ 210	1170 $\pm$ 30
58 642.35	+60	4020 $\pm$ 310	2290 $\pm$ 230	7610 $\pm$ 430	3910 $\pm$ 870	5630 $\pm$ 420	1100 $\pm$ 160	960 $\pm$ 60
58 644.32	+62	3790 $\pm$ 230	2880 $\pm$ 210	6980 $\pm$ 370	3920 $\pm$ 840	6810 $\pm$ 430	1100 $\pm$ 130	750 $\pm$ 60
58 655.19	+73	$\dots$	2440 $\pm$ 420	7260 $\pm$ 810	15080 $\pm$ 3310	14100 $\pm$ 930	1400 $\pm$ 120	1060 $\pm$ 70
58 656.12	+74	$\dots$	2170 $\pm$ 260	8940 $\pm$ 770	5800 $\pm$ 530	11110 $\pm$ 730	1150 $\pm$ 110	1070 $\pm$ 70
58 657.09	+75	$\dots$	1970 $\pm$ 190	6980 $\pm$ 420	5750 $\pm$ 750	12140 $\pm$ 740	1220 $\pm$ 90	1050 $\pm$ 70
58 658.14	+76	$\dots$	2360 $\pm$ 180	10760 $\pm$ 360	5450 $\pm$ 810	8740 $\pm$ 690	850 $\pm$ 90	1060 $\pm$ 70
58 676.19	+94	$\dots$	2040 $\pm$ 180	8720 $\pm$ 420	6640 $\pm$ 450	12490 $\pm$ 710	1160 $\pm$ 90	1100 $\pm$ 70
58 678.10	+96	$\dots$	2710 $\pm$ 240	8050 $\pm$ 500	11200 $\pm$ 1330	13200 $\pm$ 890	1310 $\pm$ 90	1120 $\pm$ 80
58 689.25	+107	3040 $\pm$ 400	2590 $\pm$ 210	10300 $\pm$ 440	4830 $\pm$ 850	11450 $\pm$ 1370	1320 $\pm$ 130	1020 $\pm$ 70
58 690.11	+108	$\dots$	2190 $\pm$ 300	6930 $\pm$ 510	3950 $\pm$ 950	12580 $\pm$ 1040	1210 $\pm$ 110	1110 $\pm$ 80
58 692.12	+110	$\dots$	2310 $\pm$ 180	7740 $\pm$ 340	8150 $\pm$ 780	12150 $\pm$ 710	1280 $\pm$ 90	1150 $\pm$ 70
58 710.94	+128	$\dots$	$\dots$	6320 $\pm$ 470	20100 $\pm$ 9500	10210 $\pm$ 850	1390 $\pm$ 130	1170 $\pm$ 80
58 715.88	+134	$\dots$	2460 $\pm$ 180	7410 $\pm$ 380	5780 $\pm$ 450	11910 $\pm$ 1250	1210 $\pm$ 90	1170 $\pm$ 70
58 717.00	+135	$\dots$	2270 $\pm$ 200	7300 $\pm$ 410	8000 $\pm$ 760	12570 $\pm$ 970	1370 $\pm$ 90	1180 $\pm$ 70
58 717.89	+135	$\dots$	1890 $\pm$ 110	6310 $\pm$ 270	4710 $\pm$ 220	$\dots$	1220 $\pm$ 40	$\dots$
58 724.14	+142	$\dots$	2160 $\pm$ 36	6370 $\pm$ 110	3570 $\pm$ 150	$\dots$	1190 $\pm$ 20	$\dots$
58 733.93	+151	$\dots$	3280 $\pm$ 550	7440 $\pm$ 1020	5470 $\pm$ 1030	10140 $\pm$ 1010	1210 $\pm$ 150	1180 $\pm$ 80
58 735.96	+153	$\dots$	2420 $\pm$ 290	7630 $\pm$ 600	8610 $\pm$ 1110	13100 $\pm$ 1110	1290 $\pm$ 100	1170 $\pm$ 80
58 777.02	+195	$\dots$	2510 $\pm$ 300	11730 $\pm$ 780	$\dots$	$\dots$	1800 $\pm$ 150	1100 $\pm$ 60
58 808.04	+226	$\dots$	2200 $\pm$ 390	13000 $\pm$ 1310	$\dots$	$\dots$	1520 $\pm$ 90	$\dots$
58 824.83	+242	$\dots$	$\dots$	$\dots$	$\dots$	$\dots$	$\dots$	1260 $\pm$ 50
58 827.82	+245	$\dots$	$\dots$	$\dots$	$\dots$	$\dots$	$\dots$	1230 $\pm$ 60
58 994.00	+411	$\dots$	1860 $\pm$ 160	$\dots$	$\dots$	$\dots$	1190 $\pm$ 60	1170 $\pm$ 50

Notes: (1) Modified Julian Date of the observations, (2) days passed from the discovery of the transient, MJD 58 582.46.

**Table B2.** Equivalent Width of the emission lines, in  $\text{\AA}$ . With  $\dots$  we indicate an epoch in which the line in question could not be fit.

MJD <sup>(1)</sup>	phase <sup>(2)</sup>	H $\delta$	H $\gamma$	He II	H $\beta$ broad	H $\alpha$ broad	H $\beta$ narrow	H $\alpha$ narrow
58 616.36	+34	9.0 $\pm$ 1.0	10.8 $\pm$ 1.1	44.6 $\pm$ 2.2	15.1 $\pm$ 3.1	33.5 $\pm$ 3.6	11.1 $\pm$ 1.2	43.0 $\pm$ 1.0
58 631.13	+49	13.2 $\pm$ 0.7	8.5 $\pm$ 0.6	14.2 $\pm$ 1.0	5.8 $\pm$ 4.3	23.6 $\pm$ 2.5	6.6 $\pm$ 2.1	36.8 $\pm$ 1.1
58 638.28	+55	$\dots$	$\dots$	17.6 $\pm$ 1.9	8.7 $\pm$ 2.6	15.6 $\pm$ 2.6	4.4 $\pm$ 1.0	29.8 $\pm$ 1.2
58 642.35	+60	9.4 $\pm$ 0.9	5.8 $\pm$ 0.7	19.3 $\pm$ 1.4	7.1 $\pm$ 3.4	16.3 $\pm$ 2.0	8.4 $\pm$ 1.4	26.0 $\pm$ 0.9
58 644.32	+62	11 $\pm$ 0.8	8.0 $\pm$ 0.7	18.9 $\pm$ 1.3	7.2 $\pm$ 3.0	21.9 $\pm$ 2.0	9.3 $\pm$ 1.2	35.3 $\pm$ 0.9
58 655.19	+73	$\dots$	6.2 $\pm$ 1.3	13.4 $\pm$ 2.1	24.3 $\pm$ 5.9	36.4 $\pm$ 3.0	11.2 $\pm$ 0.9	37.3 $\pm$ 0.8
58 656.12	+74	$\dots$	7.6 $\pm$ 1.1	15.5 $\pm$ 1.7	15.7 $\pm$ 2.3	35.1 $\pm$ 3.0	11.6 $\pm$ 0.9	47.4 $\pm$ 1.0
58 657.09	+75	$\dots$	6.8 $\pm$ 0.8	14.4 $\pm$ 1.1	8.0 $\pm$ 1.7	40.8 $\pm$ 3.1	12.2 $\pm$ 0.6	49.5 $\pm$ 1.0
58 658.14	+76	$\dots$	8.9 $\pm$ 0.8	36.8 $\pm$ 1.5	6.6 $\pm$ 1.5	22.5 $\pm$ 2.4	7.5 $\pm$ 0.5	47.0 $\pm$ 0.9
58 676.19	+94	$\dots$	6.7 $\pm$ 0.6	18.5 $\pm$ 1.1	16.5 $\pm$ 1.6	39.9 $\pm$ 2.9	9.6 $\pm$ 0.5	48.2 $\pm$ 0.8
58 678.10	+96	$\dots$	7.5 $\pm$ 0.8	16.8 $\pm$ 1.2	20.6 $\pm$ 2.7	38.9 $\pm$ 3.3	9.6 $\pm$ 0.5	43.1 $\pm$ 1.0
58 689.25	+107	4.9 $\pm$ 0.8	7.9 $\pm$ 0.7	28.5 $\pm$ 1.6	8.6 $\pm$ 2.9	23.4 $\pm$ 3.6	10.3 $\pm$ 1.2	38.8 $\pm$ 1.1
58 690.11	+108	$\dots$	5.2 $\pm$ 0.9	12.8 $\pm$ 1.2	4.3 $\pm$ 2.0	32.3 $\pm$ 3.5	8.9 $\pm$ 0.9	45.6 $\pm$ 1.1
58 692.12	+110	$\dots$	6.9 $\pm$ 0.6	17.0 $\pm$ 1.1	13.0 $\pm$ 1.7	35.1 $\pm$ 2.7	11.0 $\pm$ 0.5	49.0 $\pm$ 0.8
58 710.94	+128	$\dots$	5.5 $\pm$ 2.0	13.1 $\pm$ 4.3	37.6 $\pm$ 20.0	30.4 $\pm$ 3.5	12.9 $\pm$ 1.2	50.3 $\pm$ 1.2
58 715.88	+134	$\dots$	8.4 $\pm$ 0.7	14.9 $\pm$ 1.0	10.6 $\pm$ 1.3	22.6 $\pm$ 3.1	9.1 $\pm$ 0.5	43.7 $\pm$ 0.9
58 717.00	+135	$\dots$	6.1 $\pm$ 0.6	12.8 $\pm$ 0.9	10.9 $\pm$ 1.5	26.7 $\pm$ 2.6	8.8 $\pm$ 0.4	41.4 $\pm$ 0.8
58 717.89	+135	$\dots$	9.6 $\pm$ 1.6	23.0 $\pm$ 1.5	20.9 $\pm$ 1.6	$\dots$	14.3 $\pm$ 0.6	$\dots$
58 724.14	+142	$\dots$	7.3 $\pm$ 0.2	15.9 $\pm$ 0.4	5.8 $\pm$ 0.5	$\dots$	9.1 $\pm$ 0.2	$\dots$
58 733.93	+151	$\dots$	8.1 $\pm$ 1.7	13.3 $\pm$ 2.4	11.0 $\pm$ 3.3	24.9 $\pm$ 3.4	9.1 $\pm$ 1.1	53.0 $\pm$ 1.2
58 735.96	+153	$\dots$	6.5 $\pm$ 0.9	13.9 $\pm$ 1.4	12.2 $\pm$ 2.1	38.7 $\pm$ 4.2	10.9 $\pm$ 0.6	61.4 $\pm$ 1.5
58 777.02	+195	$\dots$	4.2 $\pm$ 0.6	15.5 $\pm$ 1.3	$\dots$	$\dots$	11.5 $\pm$ 0.5	41.1 $\pm$ 0.9
58 808.04	+226	$\dots$	3.4 $\pm$ 0.7	14.8 $\pm$ 1.9	$\dots$	$\dots$	10.1 $\pm$ 0.6	$\dots$
58 824.83	+242	$\dots$	$\dots$	$\dots$	$\dots$	$\dots$	$\dots$	45.2 $\pm$ 1.0
58 827.82	+245	$\dots$	$\dots$	$\dots$	$\dots$	$\dots$	$\dots$	46.7 $\pm$ 1.2
58 994.00	+411	$\dots$	4.6 $\pm$ 0.5	$\dots$	$\dots$	$\dots$	13.6 $\pm$ 0.5	65.9 $\pm$ 2.6

Notes: (1) Modified Julian Date of the observations, (2) days passed from the discovery of the transient, MJD 58 582.46.



**Table B3.** Shift with respect to the restframe wavelength of the emission lines, in  $\text{km s}^{-1}$ . With  $\dots$  we indicate an epoch in which the line in question could not be fit. The narrow peaks of H $\alpha$  and H $\beta$  are not listed, as we assumed they were at the restframe and we used their offset to probe uncertainties in the wavelength calibration.

MJD <sup>(1)</sup>	phase <sup>(2)</sup>	H $\delta$	H $\gamma$	He II	H $\beta$ broad <sup>(3)</sup>	H $\alpha$ broad
58 616.36	+34	240 $\pm$ 330	170 $\pm$ 310	-1770 $\pm$ 320	20 $\pm$ 300	-170 $\pm$ 460
58 631.13	+49	230 $\pm$ 310	630 $\pm$ 300	-1440 $\pm$ 320	420 $\pm$ 300	-220 $\pm$ 370
58 638.28	+55	$\dots$	$\dots$	-2410 $\pm$ 360	-200 $\pm$ 300	-1560 $\pm$ 460
58 642.35	+60	-460 $\pm$ 320	310 $\pm$ 310	-2670 $\pm$ 330	-60 $\pm$ 300	-760 $\pm$ 350
58 644.32	+62	-36 $\pm$ 310	150 $\pm$ 310	-2250 $\pm$ 320	-100 $\pm$ 300	-380 $\pm$ 340
58 655.19	+73	$\dots$	-72 $\pm$ 340	-1960 $\pm$ 470	-400 $\pm$ 300	-1820 $\pm$ 440
58 656.12	+74	$\dots$	-200 $\pm$ 310	-1190 $\pm$ 420	-320 $\pm$ 290	-690 $\pm$ 390
58 657.09	+75	$\dots$	240 $\pm$ 300	-1860 $\pm$ 330	-180 $\pm$ 290	-840 $\pm$ 390
58 658.14	+76	$\dots$	130 $\pm$ 300	-260 $\pm$ 320	-140 $\pm$ 290	-1190 $\pm$ 380
58 676.19	+94	$\dots$	80 $\pm$ 300	-1630 $\pm$ 330	-280 $\pm$ 290	-820 $\pm$ 390
58 678.10	+96	$\dots$	-100 $\pm$ 310	-2270 $\pm$ 370	-420 $\pm$ 290	-1390 $\pm$ 420
58 689.25	+107	370 $\pm$ 330	480 $\pm$ 300	-2740 $\pm$ 340	-90 $\pm$ 300	40 $\pm$ 540
58 690.11	+108	$\dots$	55 $\pm$ 320	-2670 $\pm$ 340	-380 $\pm$ 290	-760 $\pm$ 460
58 692.12	+110	$\dots$	9 $\pm$ 300	-1850 $\pm$ 330	-370 $\pm$ 290	-930 $\pm$ 390
58 710.94	+128	$\dots$	$\dots$	-2350 $\pm$ 490	-450 $\pm$ 300	-600 $\pm$ 410
58 715.88	+134	$\dots$	350 $\pm$ 300	-1590 $\pm$ 320	-150 $\pm$ 290	-2890 $\pm$ 550
58 717.00	+135	$\dots$	69 $\pm$ 300	-1750 $\pm$ 330	-230 $\pm$ 290	-900 $\pm$ 440
58 717.89	+135	$\dots$	240 $\pm$ 60	-2530 $\pm$ 70	-60 $\pm$ 60	$\dots$
58 724.14	+142	$\dots$	210 $\pm$ 17	-2250 $\pm$ 30	-460.1 $\pm$ 40	$\dots$
58 733.93	+151	$\dots$	620 $\pm$ 360	-1050 $\pm$ 460	-250 $\pm$ 300	-880 $\pm$ 450
58 735.96	+153	$\dots$	330 $\pm$ 320	-1300 $\pm$ 370	-90 $\pm$ 290	-1470 $\pm$ 480
58 777.02	+195	$\dots$	380 $\pm$ 320	-3550 $\pm$ 380	$\dots$	$\dots$
58 808.04	+226	$\dots$	-230 $\pm$ 330	-3540 $\pm$ 500	$\dots$	$\dots$
58 824.83	+242	$\dots$	$\dots$	$\dots$	$\dots$	$\dots$
58 827.82	+245	$\dots$	$\dots$	$\dots$	$\dots$	$\dots$
58 994.00	+411	$\dots$	150 $\pm$ 300	$\dots$	$\dots$	$\dots$

Notes: (1) Modified Julian Date of the observations, (2) days passed from the discovery of the transient, MJD 58 582.46. (3) The central wavelength of the broad H $\beta$  has been tied to the one of the narrow peak during the fitting procedure.

Table C1. Extinction corrected, AB magnitudes

MJD <sup>(1)</sup>	seeing ["]	w2	m2	w1	U	B	g
58 619.12*	1.9	...	...	...	...	...	16.57 ± 0.06
58 620.71*	2.4	...	...	...	...	16.74 ± 0.08	16.56 ± 0.06
58 620.18	...	16.46 ± 0.05	16.82 ± 0.06	16.83 ± 0.07	16.96 ± 0.09	16.50 ± 0.09	...
58 621.07*	2.4	...	...	...	...	16.69 ± 0.10	16.48 ± 0.06
58 624.08	...	16.56 ± 0.05	16.82 ± 0.06	16.92 ± 0.08	17.22 ± 0.11	16.66 ± 0.10	...
58 627.21	...	16.66 ± 0.05	16.82 ± 0.05	17.00 ± 0.07	17.11 ± 0.09	16.74 ± 0.10	...
58 627.80*	1.9	...	...	...	...	16.93 ± 0.08	16.64 ± 0.06
58 630.32	...	16.71 ± 0.05	16.84 ± 0.05	17.03 ± 0.07	17.09 ± 0.09	16.74 ± 0.09	...
58 633.52	...	16.61 ± 0.06	16.86 ± 0.07	17.09 ± 0.10	17.24 ± 0.13	16.75 ± 0.13	...
58 636.10	...	16.76 ± 0.05	17.14 ± 0.05	17.13 ± 0.07	17.33 ± 0.09	16.86 ± 0.09	...
58 639.27*	2.2	...	...	...	...	...	16.60 ± 0.06
58 639.83	...	16.81 ± 0.04	17.09 ± 0.05	17.09 ± 0.06	17.30 ± 0.07	16.91 ± 0.08	...
58 642.40	...	16.84 ± 0.04	17.08 ± 0.05	17.19 ± 0.06	17.35 ± 0.08	16.96 ± 0.08	...
58 645.32	...	16.88 ± 0.05	17.16 ± 0.06	17.19 ± 0.07	17.42 ± 0.10	16.87 ± 0.09	...
58 647.69*	2.2	...	...	...	...	16.95 ± 0.08	16.66 ± 0.05
58 648.79	...	16.98 ± 0.05	17.19 ± 0.06	17.17 ± 0.07	17.30 ± 0.09	16.85 ± 0.09	...
58 653.58	...	17.07 ± 0.07	17.17 ± 0.07	17.29 ± 0.09	17.46 ± 0.12	16.90 ± 0.12	...
58 655.09*	2.8	...	...	...	...	16.78 ± 0.11	16.54 ± 0.10
58 656.04+	1.1	...	...	...	...	16.97 ± 0.07	16.64 ± 0.09
58 661.07+	1.0	...	...	...	...	16.98 ± 0.07	16.68 ± 0.07
58 661.75*	2.4	...	...	...	...	16.98 ± 0.07	16.59 ± 0.05
58 665.42*	2.4	...	...	...	...	17.01 ± 0.07	16.62 ± 0.05
58 667.10+	1.1	...	...	...	...	16.96 ± 0.07	16.69 ± 0.08
58 672.13+	1.3	...	...	...	...	16.98 ± 0.08	16.74 ± 0.06
58 675.16	...	17.38 ± 0.07	17.71 ± 0.08	17.67 ± 0.10	17.68 ± 0.13	16.90 ± 0.11	...
58 675.95*	2.1	...	...	...	...	17.10 ± 0.08	16.74 ± 0.06
58 680.19	...	17.48 ± 0.06	17.87 ± 0.07	17.75 ± 0.08	17.90 ± 0.11	17.22 ± 0.09	...
58 682.42*	2.9	...	...	...	...	16.93 ± 0.18	16.66 ± 0.10
58 693.60	...	17.64 ± 0.06	17.99 ± 0.08	18.00 ± 0.07	...	...	...
58 695.39	...	17.94 ± 0.09	18.06 ± 0.12	18.20 ± 0.10	...	...	...
58 699.31	...	17.98 ± 0.07	18.18 ± 0.10	18.23 ± 0.08	...	...	...
58 703.44	...	17.75 ± 0.09	18.28 ± 0.14	18.06 ± 0.10	...	...	...
58 707.42	...	17.98 ± 0.08	18.23 ± 0.10	18.02 ± 0.08	...	...	...
58 712.80	...	18.22 ± 0.08	18.52 ± 0.11	18.36 ± 0.08	...	...	...
58 729.28	...	18.40 ± 0.10	...	...	...	...	...
58 731.93	...	18.12 ± 0.11	18.60 ± 0.14	18.45 ± 0.17	18.07 ± 0.18	17.12 ± 0.14	...
58 733.44	...	18.40 ± 0.14	18.49 ± 0.16	18.30 ± 0.18	18.45 ± 0.25	17.26 ± 0.17	...
58 761.06	...	18.64 ± 0.12	18.84 ± 0.13	18.55 ± 0.16	18.41 ± 0.20	17.46 ± 0.15	...
58 766.05	...	18.73 ± 0.17	19.15 ± 0.21	18.75 ± 0.23	18.20 ± 0.21	17.48 ± 0.19	...
58 771.43	...	18.67 ± 0.09	18.95 ± 0.10	18.62 ± 0.12	18.24 ± 0.12	17.13 ± 0.09	...

Notes: (1) Modified Julian Date of the observations. Epochs marked with \* indicate data from Las Cumbres, epochs marked with + indicate data from LT, the rest of the data is taken with *Swift*. For all filters the extinction correction was done using the values in [Schlafly & Finkbeiner \(2011\)](#) who assume a reddening law with  $R_V=3.1$